Analysis of cortical actin dynamics and its regulatory proteins in living cells

Yanshu ZHANG

Abstract

Intracellular actin-based architectures play critical roles in various cellular functions and events, such as cell migration, cell division, mechanical response and tissue organization. Cell cortex is composed of a random meshwork of actin filaments and other actin-related proteins, and lies beneath the plasma membrane. Due to technical limitations, the molecular mechanism maintaining and regulating the cortical actin dynamics has been less understood than other actin-based architectures such as stress fibers. In this study, I tried to establish a microscope technique to visualize and analyze the dynamics of individual actin filaments in a living cell cortex by utilizing high-speed atomic force microscope (HS-AFM), and applied it for functional analyses of actin-regulating proteins.

I used a tip-scan type HS-AFM to visualize actin filaments in the cell cortex by applying slightly deeper indentation of the probe into the cell to obtain higher contrast of actin filaments, which is stiffer than the plasma membrane. This allowed visualization of individual actin filaments in various cell types. The detailed analyses of obtained images elucidated several kinetic parameters in a living COS-7 cell such as elongation rate and the frequency of new filament assembly. By using inhibitors and overexpression of actin-binding proteins, a dynamic equilibrium between G-actin and F-actin in the cortex has been elucidated, which is different from that of other actin-based architectures.

Combining this system with the other microscopic techniques, I tried to examine how transcription co-factor YAP, a well-known mechano-responsive regulator, controls cortical actin structures. HS-AFM analyses and other mechanical characterizations of YAP-knock out cells revealed that, the depletion of YAP increased the density of actin filaments, the stiffness of the cell cortex, and resistance against external damages. Additional biochemical and microscopic analyses suggested the involvement of E-cadherin, one of the genes regulated by YAP, in recruiting one of the Rho GTPase-activating enzymes, ARHGAP18, to the cell cortex, which inactivates RhoA. All of these results demonstrated a linkage between transcriptional control by YAP and structural changes of cortical actin via Rho GTPases, and demonstrated that HS-AFM-based visualization approach is a powerful tool to analyze the dynamics of cortical actin network and the function of regulatory proteins.

Table of Contents

Abbreviation

AFH1	*Arabidopsis* formin 1
Aip1	Actin-interacting protein 1
ARHGAP18	Rho GTPase-activating protein 18
ARHGAP28	Rho GTPase-activating protein 28
ARHGAP29	Rho GTPase-activating protein 29
Arp2/3	Actin-related protein 2/3 complex
DMEM	Dulbecco's Modified Eagle's Medium
ECFCs	Endothelial colony forming cells
ECM	Extracellular matrix
EGFP	Enhanced green fluorescent protein
ERM	Ezrin, radixin and moesin
F-actin	Fibrous actin
FBS	Fetal bovine serum
FHOD1	Formin homology 2 domain containing protein 1
FLAP	Fluorescence localization after photobleaching
FMNL2 and 3	Formin-like family membrane 2 and 3
Formins	Formin homology proteins
FRAP	Fluorescence recovery after photobleaching
FRSK	Fetal rat skin keratinocyte cell
G-actin	Globular actin
GST	Glutathione S-transferase
HS-AFM	High-speed atomic force microscope
LIMK	LIM domain kinase
MDCK	Madin-Darby canine kidney cell
MLCP	Myosin light chain phosphatase
NRK	Normal rat kidney fibroblast cell
NUAK2	NUAK family SNF1-like kinase 2
PI	Propidium iodide
ROCK	Rho-associated protein kinase
RPE	Retinal pigment epithelial cell
SiMS	Single-molecule speckle microscopy
TAZ	Transcriptional coactivator with PDZ-binding motif
TIRFM	Total internal reflection fluorescence microscopy
YAP	Yes-associated protein 1

Chapter 1

Introduction

1.1 Actin dynamics and architectures

1.1.1 Actin is a dynamic cytoskeletal structure

Actin is a protein widely distributed in animal cells, and forms a variety of skeletal architectures within the cell. It exists in a monomeric form (G-actin) and a polymeric form (F-actin) and a transition between these two forms is equilibrated and regulated by a number of cellular proteins (Blanchoin et al., 2014).

The assembly of a single F-actin includes the steps of nucleation, elongation, and a steady state (**Fig. 1**). Nucleation is a step in which three G-actin monomers form a complex. Since this step is thermodynamically unpreferable, several nucleators facilitate this process with different mechanisms. Arp2/3 complex binds to F-actin and nucleates a branched new filament (Mullins et al., 1998). Members of formin family proteins promote an efficient nucleation by stabilizing actin dimer and trimer (Pruyne et al., 2002). Spire and cordon-bleu assemble free G-actin molecules to promote the nucleation (Quinlan et al., 2005, Ahuja et al., 2007). During the elongation step, actin monomer binds to the end of the pre-formed actin filament. Since F-actin is a directional polymer which carries structurally different ends (plus end and minus end), the affinity of G-actin to the plus and minus ends is different, which results in different polymerization kinetics at each end. Formins associate with the F-actin plus ends and modify its elongation rate together with profilin (Vavylonis et al., 2006). Profilin binds to G-actin and controls formin-dependent

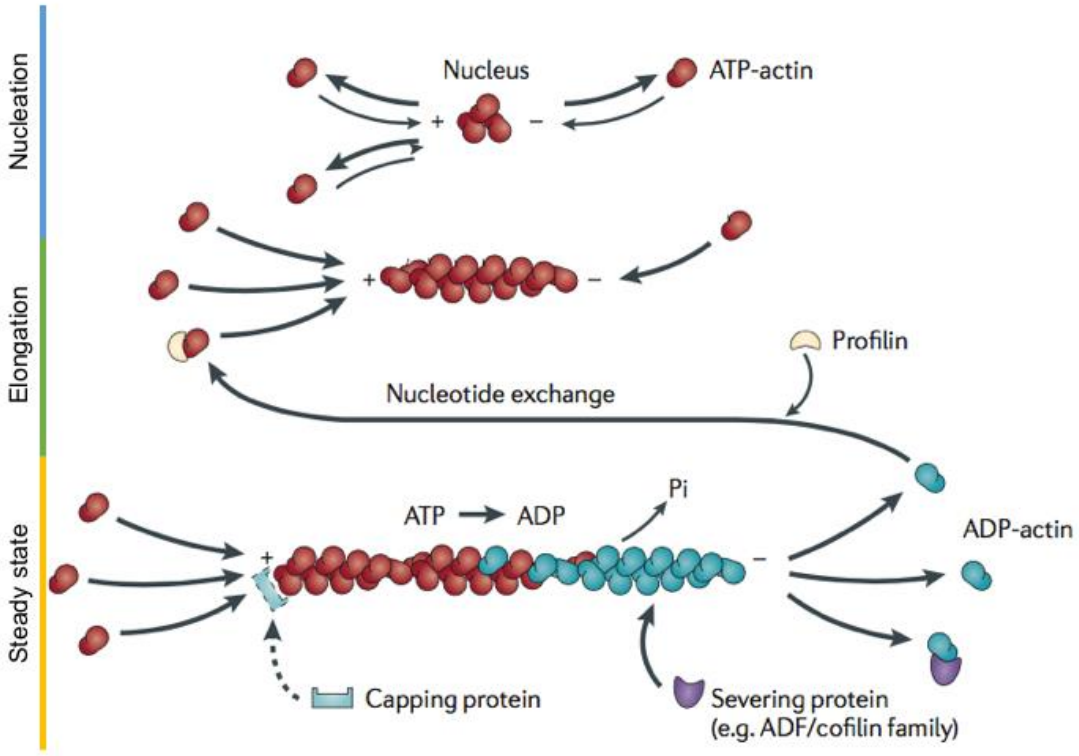

Fig 1. Actin filament assembly

Actin filament assembly includes the nucleation, elongation and a steady state. During this process, G-actin bound ATP is hydrolyzed to ADP after actin polymerization. Actin-binding proteins such as capping protein, ADF/cofilin control the assembly and disassembly of actin filaments. Image was adapted from Alexander Nürnberg et al., 2011

elongation of F-actin (Pernier et al., 2016). Ena/VASP increases the elongation rate by preventing capping proteins from binding to the plus end (Barzik et al., 2005; Breitsprecher et al., 2011). When the reaction reaches a steady state, the assembly and disassembly are balanced. The members of actin-depolymerizing factor (ADF)/cofilin family proteins bind to F-actin (preferably to ADP-bound actin), destabilize it, and accelerate the severing of the filament (Carlier et al., 1997). Actin interacting protein 1 (Aip1) is known to promote this cofilin-dependent severing process (Nadkarni and Brieher, 2014; Chen et al., 2015).

1.1.2 Actin forms various architectures in the cell

In addition to polymerization/depolymerization dynamics of a single actin filament, multiple filaments are assembled to build up higher-order architectures in the cell. Arp2/3 makes a branching point on the pre-formed filament and nucleates a new filament (Mullins et al., 1998). Filamin crosslinks actin filaments to form angled actin network (Nakamura et al., 2002), and AFH1, one of the formin family members in *Arabidopsis*, facilitates the formation of parallel and antiparallel actin bundles (Michelot et al., 2006), whereas fascin makes parallel actin bundles (Jansen et al., 2011).

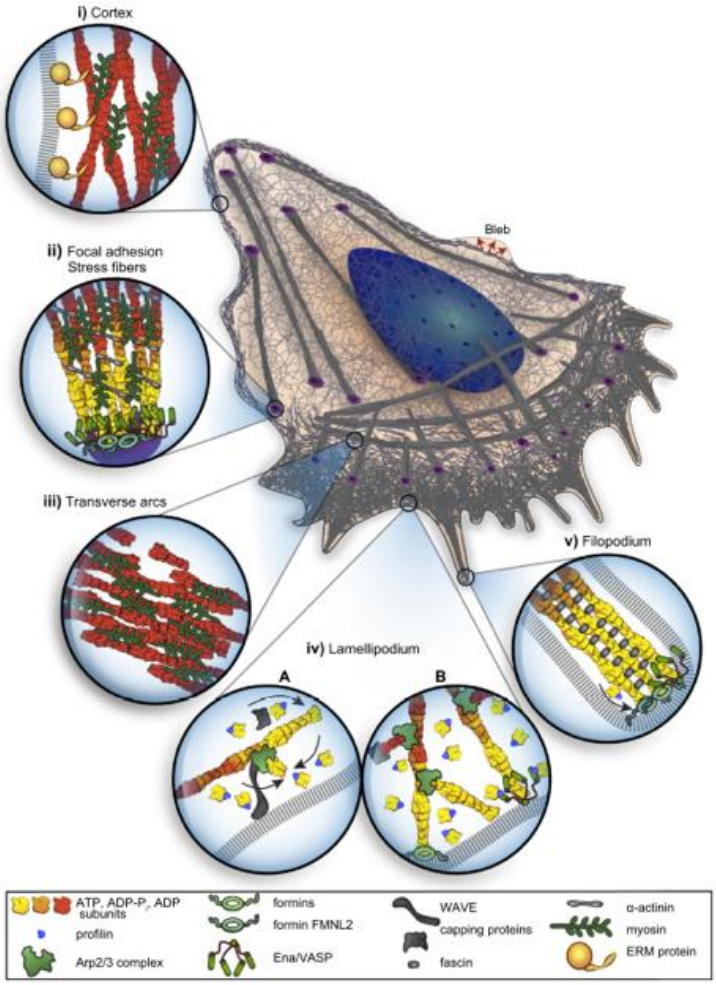

Fig 2. Actin architectures in cells

Actin forms the lamellipodia, filopodia, stress fibers and cortex in the cells. Lamellipodia are broad protrusions at the leading edge of a migrating cell, filopodia are finger-like protrusions formed by parallel actin bundles. Stress fibers are associated with focal adhesions to connect the cell with ECM. Cortex is a layer of actin filament meshwork associated with numerous actin binding proteins under the plasma membrane. These architectures in the cell are made up by a variety of actin structures associating with various actin-binding proteins.

Image was adapted from Blanchoin et al., 2014

The assembly of such higher-order network of actin filaments finally constructs various functional architectures in the cells, such as lamellipodia, filopodia, stress fibers, and cortex (**Fig. 2**). Lamellipodia are thin and broad protrusions of the cell edge made by a number of branched actin filaments. They are often found at the leading edge of a migrating cell, and contains a number of branched actin filaments made by Arp2/3 complex (Krause and Gautreau, 2014). Filament elongation at a number of plus ends pushes the plasma membrane outwards, and generates force to extend the lamellipodia (Suraneni et al., 2012). Formins (FMNL2 and 3) (Kage et al., 2017) and Ena/VASP (Bear et al., 2002) facilitate the filament elongation at the plus end.

In contrast to lamellipodia, filopodia are finger-like protrusions which are made up of parallel actin bundles (Gupton and Gertler, 2007). Ena/VASP plays a role in making a long and unbranched actin filaments and bundles (Lebrand et al., 2004; Schirenbeck et al., 2006). mDia2, a member of formin family, also facilitates the elongation of F-actin at the tip of the filopodia (Yang et al., 2007), and fascin bundles and stabilizes those filaments (Pfisterer et al., 2020). Stress fibers contain actin bundles of around 10-30 filaments (Cramer et al., 1997), associate with focal adhesions, and generate cellular tension (Parsons et al., 2010). Non-muscle myosin II assembles individual actin filaments into a thicker bundle (Goeckeler et al., 2008), and actinin bridges those bundles to

stabilize them (Tojkander et al., 2012). Cortex is a layer of actin filament meshwork associated with numerous actin binding proteins such as mDia1, mDia3 and Arp2/3 under the plasma membrane (Chugh and Paluch, 2018).

These actin architectures play diverse roles to maintain proper cellular functions. Lamellipodia direct the cell migration, and filopodia sense the guidance cues during growth cone pathfinding. The focal adhesions connect stress fibers to the extracellular matrix (ECM). The cell cortex controls the cell surface tension both in interphase and mitosis, and participates in the plasma membrane deformation such as cell wound repair and endocytosis (Katoh et al., 1995; Qualmann et al., 2000; Geraldo and Gordon-Weeks, 2009; Stewart et al., 2011; Aihara et al., 2018; Svitkina, 2018).

1.2 Cortical actin

1.2.1 Function of cortical actin

The function and importance of the cell cortex have been studied in various research fields for decades. It maintains cellular morphology and mechanics. For example, the cellular rounding force during mitosis is controlled by cortical actomyosin system and osmotic pressure (Stewart et al., 2011). During cytokinesis, the cortical actin filaments form a contractile ring to constrict the cell into two daughter cells (Cao and Wang, 1990). The cortical actin rearrangement is also required for the cell wound repair (Abreu-Blanco et

al., 2011), and endocytosis (Smythe and Ayscough, 2006), both of which are tightly coupled with morphological changes of the plasma membrane.

1.2.2 Regulators of cortical actin

Several actin-regulating proteins mentioned above are known to regulate cortical actin dynamics. Some members of formin family (mDia1 and mDia3) promote the nucleation and elongation of actin filaments to maintain a dense actin meshwork (Fritzsche et al., 2016; Sakamoto et al., 2018). Arp2/3 also nucleates new actin filaments in the cortex (Fritzsche et al., 2016). Cofilin and capping protein are known to regulate the length of cortical actin filaments, the thickness of the cortical layer and the surface tension in mitosis (Chugh et al., 2017). Myosin II stabilizes the cell cortex by crosslinking actin filaments (Laevsky and Knecht, 2003). Moesin, one of the Ezrin/Radixin/Moesin (ERM) proteins, anchors actin filaments to the plasma membrane and increased the cortical rigidity during mitosis (Kunda et al., 2008). In the upstream, small GTPases control the activity and localization of actin-related proteins. RhoA maintains the cortical rigidity during mitosis (Maddox and Burridge, 2003), and Cdc42 promotes cortical actin assembly in budding yeast (Li et al., 1995). Moreover, a transcriptional co-regulator YAP was reported to regulate the cortical actin through the small GTPases (Porazinski et al., 2015). Although some of these regulatory mechanisms are shared by those in other actin-

based structures (lamellipodia and stress fibers), the molecular mechanism of how the activities of such a large number of regulatory proteins are integrated to maintain various architectures in different intracellular locations is not fully understood.

1.2.3 Structure and dynamics of cortical actin

The structure of the cortical actin has been elucidated mainly by microscopic observations. In contrast to other actin-based architectures, actin filaments in the cortex are arranged into a random mesh-like network. The electron tomography revealed a variety of mesh sizes ranging from 50 (for fetal rat skin keratinocyte (FRSK) cells) to 200 nm (for normal rat kidney fibroblast (NRK) cells) (Morone et al., 2006). Observation by atomic force microscope (AFM) revealed a mesh size around 100 nm in NIH-3T3 cells (Eghiaian et al., 2015). The thickness of the cortex in mitotic HeLa cell was estimated as ~190 nm (Clark et al., 2013). The tension and the stiffness are the center of attention in the study of the cell cortex. Force measurement by AFM (Chugh et al., 2017) and micropipette aspiration (Thoumine et al., 1999) were common experimental methods to estimate the cell surface tension, which ranges from 35 to 1600 pN/μm depending on the cell lines, cell cycle (interphase or metaphase) and the method of measurement (Evans and Yeung, 1989; Thoumine et al., 1999; Fischer-Friedrich et al., 2014; Cartagena-Rivera et al., 2016). Fluorescence microscope-based techniques contributed to the characterization of actin in

the cell cortex. Fluorescence after photobleaching (FRAP) and fluorescence loss in photobleaching (FLIP) revealed two populations of actin filaments existing in the cortex (Fritzsche et al., 2013). Single molecule fluorescence imaging technique combined with stochastic simulation showed a formin-mediated elongation rate at the barbed end of 136 ± 14 sub/s, and an Arp2/3-mediated elongation rate of 28 ± 2 sub/s in HeLa cells (Fritzsche et al., 2016).

1.3 Goal of this study

In spite of a number of important roles of cortical actin in the cellular structures, functions and activities, the mechanism of how it is regulated by other cellular proteins at the molecular level is poorly understood due to a lack of techniques to characterize the dynamics of individual actin filaments. Most of the optical microscope-based techniques mentioned above are able to reveal bulk behavior but not the dynamics of the individual filaments in the cell cortex. On the other hand, electron microscopy can resolve individual filaments, but cannot reveal their dynamics. Therefore, I thought that functional roles of various cellular proteins in the maintenance and regulation of cortical actin network will be further elucidated if the dynamics of individual actin filaments is visualized. New information on the actin dynamics obtained from such technical advancement will be able

to bridge the results from bulk and single-molecule measurements, and contribute to understand the regulatory mechanism of the cell cortex at the molecular level.

In this study, I firstly established a method for visualizing and analyzing the dynamics of cortical actin filaments in a living cell by using high-speed atomic force microscope (HS-AFM). Then, I combine this HS-AFM approach with other microscopic techniques to elucidate the molecular mechanisms of how cortical actin is regulated by regulatory proteins such as small GTPases and the upstream transcription factor YAP.

Chapter 2

Visualization and analyses of cortical actin dynamics by high-speed atomic force microscopy

2.1 Introduction

2.1.1 Microscopic observations of actin structure and dynamics

Various microscopic techniques have been utilized to observe actin structures and dynamics. Fluorescence-based techniques, such as confocal microscopy and total internal reflection fluorescence microscopy (TIRFM), visualized the dynamics of actin, and revealed the regulatory mechanisms of dorsal stress fibers (mDia1/DRF1 formin-mediated) and transverse arcs (Arp2/3-mediated polymerization combined with myosin-mediated bundling) (Hotulainen and Lappalainen, 2006). Fluorescence recovery after photo-bleaching (FRAP) and fluorescence loss in photo-bleaching (FLIP) analyses identified two subpopulations of actin filaments with different exchanging rates in the cell cortex (Fritzsche et al., 2013). Further studies using single-molecule fluorescence imaging technique clarified that one is mediated by formin (mDia1) and the other is Arp2/3-mediated (Fritzsche et al., 2016). Single-molecular speckle microscopy (SiMS) has been used to reveal a rapid actin turnover in lamellipodia of living XTC cells (Watanabe and Mitchison, 2002; Yamashiro et al., 2014). Correlative imaging of fluorescence and electron microscope revealed the molecular mechanism of the initiation step of filopodia elongation (Svitkina et al., 2003). Recent advancement in various super-resolution microscopies enabled the visualization of individual actin filaments and revealed the function of actin regulatory proteins such as formins (Sakamoto et al., 2018).

In most of the fluorescence-based microscopies, actin filaments have to be labeled by a fluorescent probe. A wide variety of fluorescent probes for actin have been developed and utilized so far. Phalloidin is a bicyclic heptapeptide which specifically binds to F-actin. Rhodamine-labeled phalloidin has been widely used to fluorescently label F-actin in a fixed cell and *in vitro*, but cannot be used for live-cell imaging. Lifeact-GFP is currently used for live-cell imaging of F-actin. It is a small peptide (17 amino acids) fused with GFP and binds to F-actin when it is expressed in a living cell (Wulf et al., 1979; Riedl et al., 2008). GFP-fused β-actin was also used for live-cell imaging. In contrast to Lifeact-GFP, it is incorporated into F-actin. However, due to its large unincorporated fraction in the cytoplasm, it has high background signal under the fluorescence observation. Fluorescently-labeled actin can also be used in live cell imaging, but has to be injected into the cell by microinjection.

In any cases of fluorescence observation described above, actin or actin-binding molecule has to be fluorescently labeled and expressed or introduced in the cell of interest. In the case of plasmid-based transfection, the expression level of such exogenous protein is difficult to be tightly controlled, and the over-expression of exogenous fraction often disturbs intracellular actin pool (G and F-actin) and the equilibrium state. These technical

problems are now being improved in recent development of new probes and techniques, but the effect of over-expression has to be carefully examined in individual cases.

2.1.2 Topographical imaging by HS-AFM

Atomic force microscope (AFM) is a scanning probe microscope, which visualizes the surface topography of the specimen by using a sharp probe. It has been used for visualization of DNA, protein and various cellular architectures. The biggest advantage of AFM is that it does not require fixation, staining or labeling of the specimen, but nevertheless has a molecular resolution in liquid. Recent advancement in the scanning speed greatly increased the temporal resolution and contributed in the imaging of molecular dynamics of a single protein, such as myosin V walking on an actin filament (Kodera et al., 2010), the rotation of $\alpha_3\beta_3$ stator ring of F_1-ATPase (Takayuki et al., 2011).

Although the HS-AFM has a great advantage in the imaging of single protein molecules, it could not be used for live-cell imaging because the sample stage, but not the probe, is scanning to x-y direction ("stage-scan" configuration). To solve this problem, a "tip-scan" type of HS-AFM unit had been developed in the lab I belong to (Suzuki et al., 2013). The AFM unit, which contains x-y-z scanner is mounted on the stage of an inverted microscope, so that a specimen (a living cell in a culture dish) can be observed by the optical system of the inverted microscope. In addition to such "tip-scan" configuration, a

phase-feedback mechanism lowered the force applied by the probe to the surface of the specimen, so that soft specimen such as a living cell membrane could be visualized in high contrast (Yoshida et al., 2015).

2.1.3 Aim of this chapter

In this chapter, I utilized this house-made HS-AFM system to visualize cortical actin filaments in a living cell. I expected that small indentation of the probe into the cell will give a high contrast image of actin filaments near the plasma membrane, since the actin filament is stiffer than the plasma membrane. As described in the following section, I successfully established a method of HS-AFM imaging and analyzing the dynamics of cortical actin at the single-filament level. Furthermore, the roles of various actin-regulating proteins such as profilin, thymosin β4, Arp2/3 complex and formins in the regulation of cortical actin were elucidated.

2.2 Materials and methods

2.2.1 Cell culture and transfection

COS-7, NIH-3T3, C2C12 cells were cultured in Dulbecco's Modified Eagle's Medium (DMEM), and ST2 cells were cultured in Roswell Park Memorial Institute (RPMI) 1640 Medium. All mediums were supplemented with 10% fetal bovine serum (FBS) and cells

were maintained in plastic culture dishes at 37 ℃ and 5% CO_2. XTC cells (a gift from Professor Watanabe, Kyoto University) were cultured in 70% Leibovitz's L-15 Medium with 10% fetal calf serum (FCS) at room temperature. The cDNA of human profilin-1 (Kazusa DNA clone #FXC06337) was cloned into pEGFP-C3 to create a fusion of profilin-1 with enhanced green fluorescent protein (EGFP). The mCherry-thymosin β4 was a gift from Dr Harata, Tohoku University. These plasmids were transfected with Effectene Transfection Reagent (Qiagen) and incubated for 24–48 hours. Cells used for AFM imaging were confirmed with fluorescence signals by confocal microscope installed in the inverted microscope of the HS-AFM unit.

2.2.2 HS-AFM

The tip-scan HS-AFM unit combined with an inverted fluorescent/optical microscope (IX83, Olympus) system (Suzuki et al., 2013) was used. The imaging technique of actin dynamics was developed based on the previous studies (Suzuki et al., 2013; Yoshida et al., 2015). A sharp cantilever tip with a spring constant of 0.1 N/m (USC-F0.8-k0.1, Nanoworld) was used. Cells were seeded on a slide glass coated with Poly-L-lysine (PLL) (Sigma) and cells attached to the glass bottom was chosen for imaging. A flat area far from the cell edge was chosen as a target based on the phase-contrast image of the cell.

AFM images were taken every 10 seconds per frame with a loading force of <85 pN. AFM images were exported to 640×480 pixels^2, and the scan area was 6×4.5 μm^2.

2.2.3 Image analysis and statistics

For image analysis, AFM images were processed with ImageJ (NIH) software. For elongation rate, the filament ends were chased in two or three consecutive images. The newly appeared actin filaments were measured by counting the new actin filaments number in an area of 1×1 μm^2 of two consecutive images and the density of actin filaments was measured as the filament number in an area of 1×1 μm^2 in AFM images. The relative vertical position of an actin filament was traced in a series of images till the filament completely become invisible. A horizontal line with respect to x-axis was drawn and the same place was tracked over time in several frames. The relative vertical position when filament appeared was set as 0. The mesh area was measured as the area that segmented by the actin filaments. And the angle of the filaments was measured as the angle with respect to the x-axis of the image that less than 90 degree. Statistical analysis was performed by Microsoft Excel software. Student's t-test was performed to compare if the difference of 2 data sets is significant or not. *, $p<0.05$

2.2.4 Drug treatment

Cytochalasin B (Sigma) was used at a concentration of 2 μM. For blebbistatin (Abcam), the concentration was 50 μM, and for jasplakinolide (Abcam), the concentration was 1 μM. For CK-666 (Sigma) the concentration was 50 μM and for SMIFH2 (Sigma) the concentration was 10.6 μM.

2.3 Results

2.3.1 Actin turnover in the cortical layer

Previous study in my laboratory demonstrated that the morphology of the cell surface significantly varies in different cell lines. For visualization of cortical actin filaments, I chose COS-7 cell, which was derived from the kidney of the African green monkey, since it is thin, flat and has smooth surface, which enables clear imaging of individual actin filaments in a living cell in high contrast.

When a COS-7 cell was visualized by HS-AFM at a frame rate of 0.1 frame/sec, a random network of actin filaments was observed, and newly assembled filaments were frequently appeared **(Fig. 3)**. To quantify and characterize the newly assembled filaments, two consecutive images (10 sec interval) were subtracted **(Fig. 4)**. The number of newly appeared actin filaments in a unit area was measured to be $1.91 \pm 0.80\ \mu m^{-2} \cdot 10\ s^{-1}$ ($0.19 \pm 0.08\ \mu m^{-2} \cdot s^{-1}$). This corresponds to approximately 15,000 filaments in a cell in a minute.

A careful analysis of AFM images revealed the elongation of a single actin filament. The rate of the elongation was measured to be 0.19 ± 0.07 μm·s^{-1} **(Fig. 5)**. To confirm this elongation was polymerization at the end of the filament but not a sliding of a filament, the cells were treated with an actin polymerization inhibitor, cytochalasin B or a non-muscle Myosin II inhibitor, blebbistatin **(Fig. 6A)**. The elongation rate as well as the density was reduced significantly by cytochalasin B, but not by blebbistatin **(Fig. 6B)**. These results demonstrated that the appearance of new actin filaments in the HS-AFM images is polymerization at the filament end.

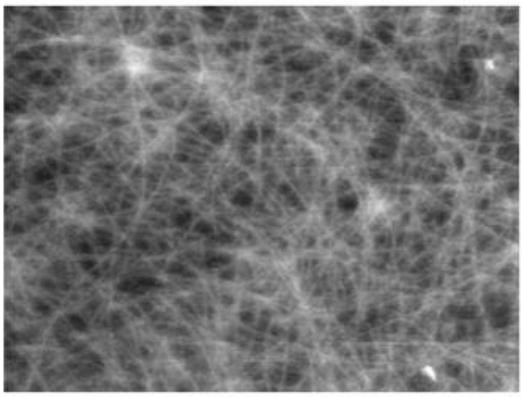

Fig 3. Snapshot of the cortical actin filaments in a living COS-7 cell taken by HS-AFM
Cortical actin filaments showed a dense meshwork in a living COS-7 cell and frequently appeared and disappeared.

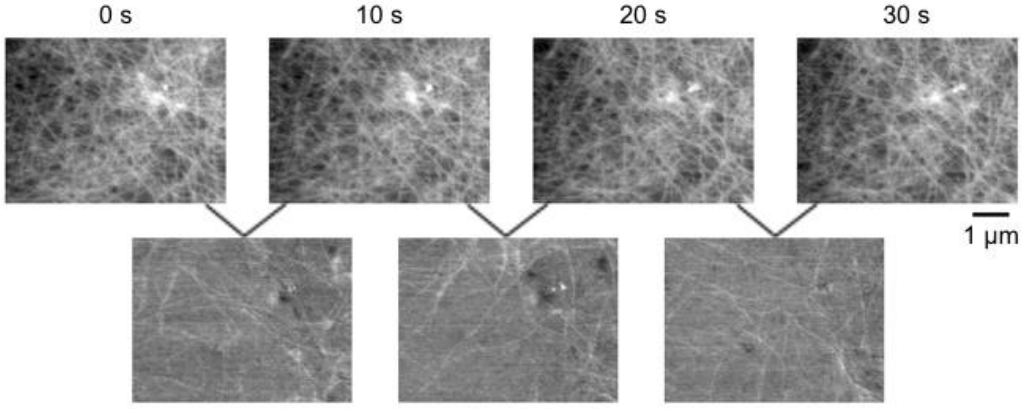

Fig 4. Subtraction of the AFM images
Subtracted signals between two consecutive AFM images are showed (down), white indicate appeared signals and black indicates the disappeared signals. The upper figures shows the original AFM images. A lot of actin filaments appeared between 2 frames in 10 seconds.

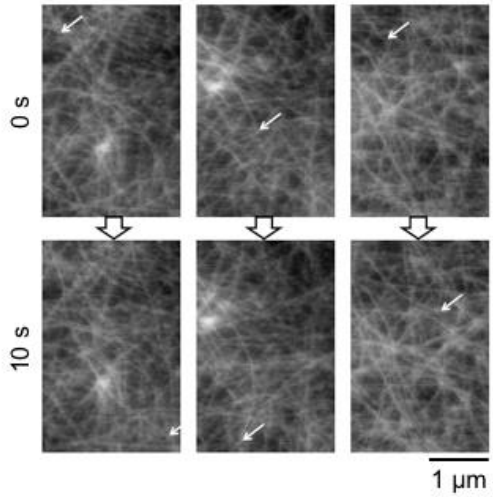

Fig 5. Elongation of actin filaments
Trace the elongation of a single actin filament between two consecutive frames in 10 seconds. The AFM images taken at 0 second (upper) and 10 seconds after the first image (down). Arrows show the ends of single actin filaments.

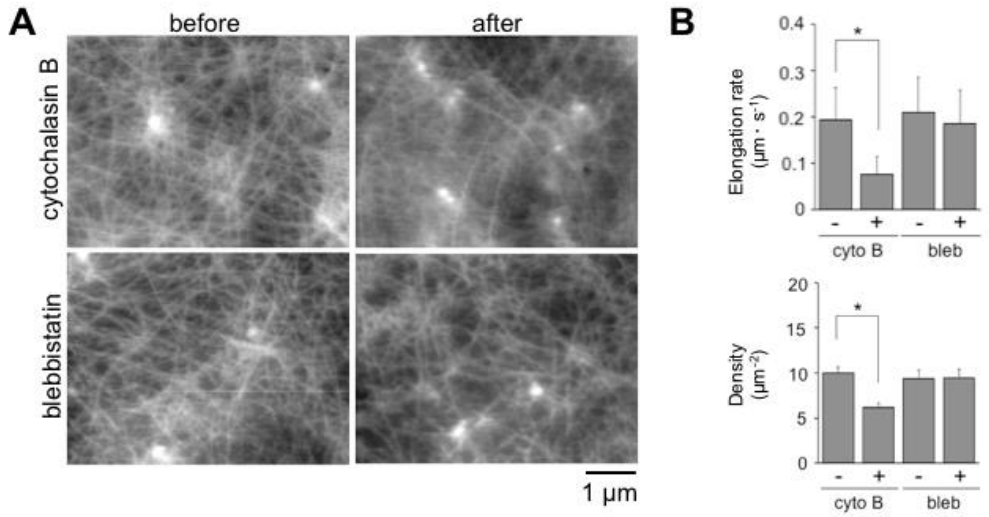

Fig 6. Cytochalasin B inhibited the elongation of filaments but not blebbistatin

(A) The cortical actin before and after the treatment of cytochalasin B and blebbistatin. The images showed the same area of the cell before and after the treatment within 5 minutes.

(B) The graph showed the elongation rate and the density of actin filaments before and after the treatment of cytochalasin B and blebbistatin. The elongation rate was obtained from >10 filaments. Error bar indicates SD. *, $p<0.05$ with two tailed t-test.

2.3.2 Variations in cortical actin dynamics in different cell types

The cortical actin dynamics and structures were also visualized and compared in different cell types: NIH-3T3 cells (a fibroblast cell line derived from a NIH Swiss mouse embryo), C2C12 cells (a myoblast cell line derived from mouse muscle), ST2 cells (a fibroblast-like cell line derived from the mouse bone marrow stroma), and XTC cells (a fibroblast cell line derived from Xenopus laevis). HS-AFM imaging of these cell lines revealed the cortical actin with diverse structures **(Fig. 7A)**. The analysis of the filament angle revealed that the orientation of actin filaments was random in COS-7, XTC, C2C12 and ST2 cells, while those in NIH-3T3 cells were oriented to the long axis of the cell **(Fig. 7C)**. The mesh area in C2C12, ST2 and XTC cells was also largely different: C2C12 cells showed the densest network with the smallest mesh area and XTC showed the largest with a broader range **(Fig. 7D)**. For the dynamics, there was a large difference in the frequency of newly assembled actin filaments; the number of newly assembled F-actin was higher in C2C12 (0.24 $\mu m^{-2} \cdot sec^{-1}$) cells and ST2 (0.19 $\mu m^{-2} \cdot sec^{-1}$), and was lowest (0.10 $\mu m^{-2} \cdot sec^{-1}$) in XTC cells **(Fig. 7B)**. In contrast, the elongation rate was not significantly different among all the cell tested **(Fig. 7B)**. These results suggested that the initiation step may be regulated by different mechanisms in different cell lines, but the elongation step promoted by a similar mechanism in these cell lines, which may be significant in the regulation of cortical actin structures.

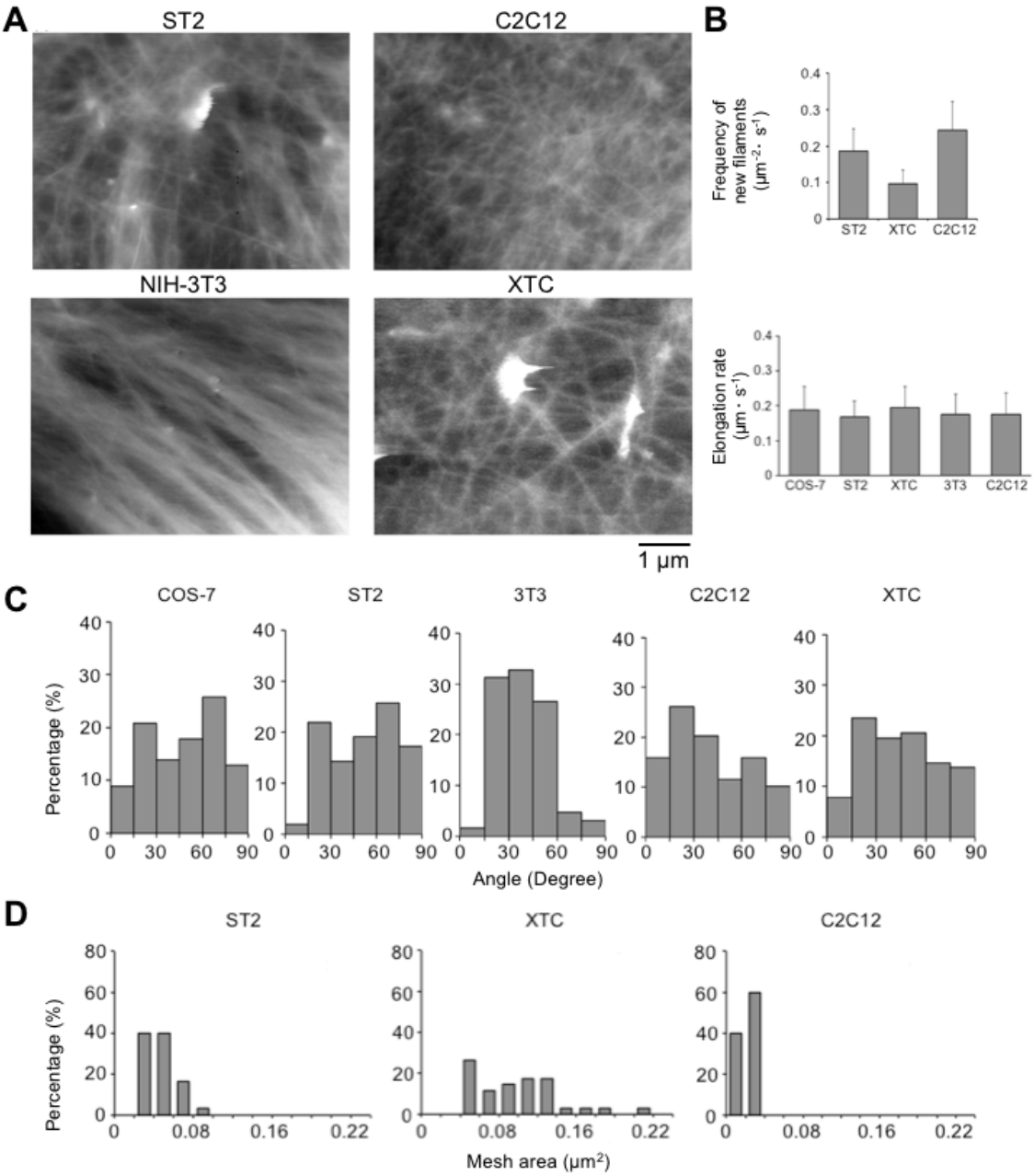

Fig 7. Different structures and dynamics revealed in different cell types

(A) The cortical actin visualized by HS-AFM in ST2, C2C12, NIH-3T3 and XTC cells.

(B) The frequency of newly assembled actin filaments and the elongation rate were analyzed and compared in different cell types. Error bar indicates SD.

(C) The angle of actin filament with respect to the horizontal axis of the image. Data was measured from >60 actin filaments for each cell line.

(D) The mesh area of cortical actin in different cell types. Data was measured from >30 regions in each cell type.

2.3.3 Maintenance of free G-actin pool in the cell cortex

To get further insight into the molecular mechanism of cortical actin regulation, the effect of various inhibitors on the actin dynamics described above (e.g., elongation rate, frequency of new filament assembly) were investigated. Jasplakinolide is a small cyclic peptide that inhibits actin depolymerization (Bubb et al., 2000). The addition of 1 μM jasplakinolide showed an immediate reduction both in the depolymerization and polymerization processes without changing the filament density **(Fig. 8A)**. After treatment, the assembly of new actin filament was rarely observed (**Fig. 8B**). The analysis of a few cases of polymerization revealed that the polymerization rate was reduced to 0.13 ± 0.04 μm·sec^{-1} **(Fig. 8B)**. This observation indicated that a small amount of free G-actin was present in the cell cortex, and it is quickly depleted by jasplakinolide, which blocks the replenishment of new G-actin into the pool.

The effect of other inhibitors on the cell cortex was investigated. Formins and Arp2/3 were previously demonstrated to be involved in actin nucleation in HeLa and M2 melanoma cells (Fritzsche et al., 2016). I tested the effects of the inhibitors of formins (SMIFH2) and Arp2/3 (CK-666). However, the treatment with SMIFH2 and CK-666 did not affect the actin filament density, the frequency of newly assembled F-actin, or the elongation rate at the cortex (**Fig. 9**). These results indicated that formins and Arp2/3 are not involved in the maintenance of cortical actin in COS-7 cells.

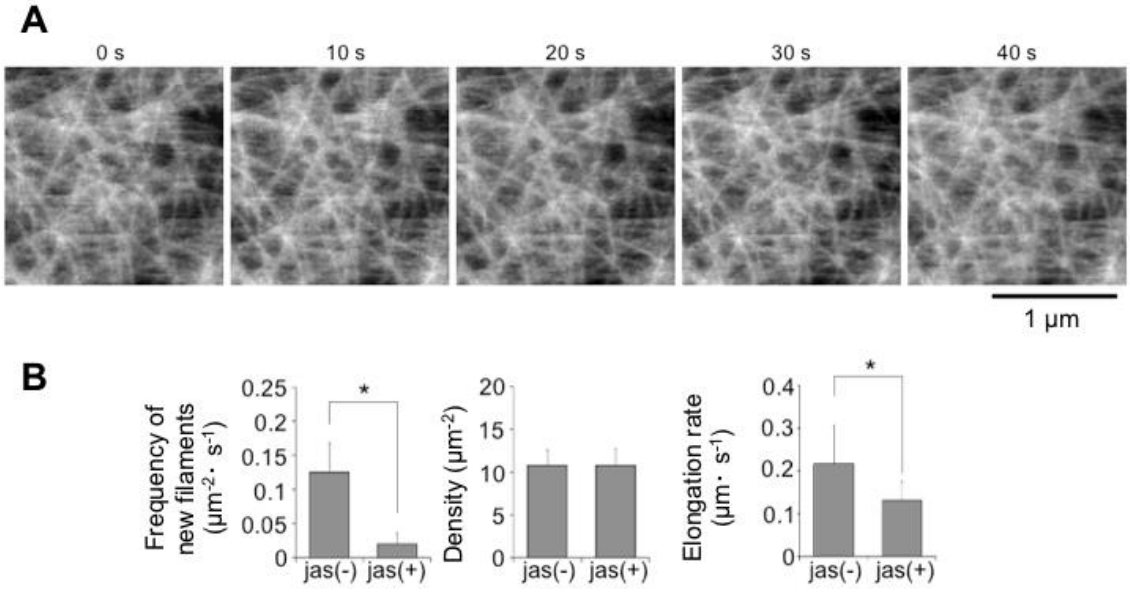

Fig 8. Cortical actin turnover inhibited by jasplakinolide

(A) Time-lapse images of cortical actin dynamics after treatment with 1 μM Jasplakinolide.

(B) Analysis of the frequency of newly assembled actin filaments, the density and the elongation rate of actin filaments. Frequency of new filament measured from 50 areas, density measured from 120 areas and elongation rate measured from >40 filaments in each condition. Error bar indicates SD. *, $p<0.05$ with two tailed t-test.

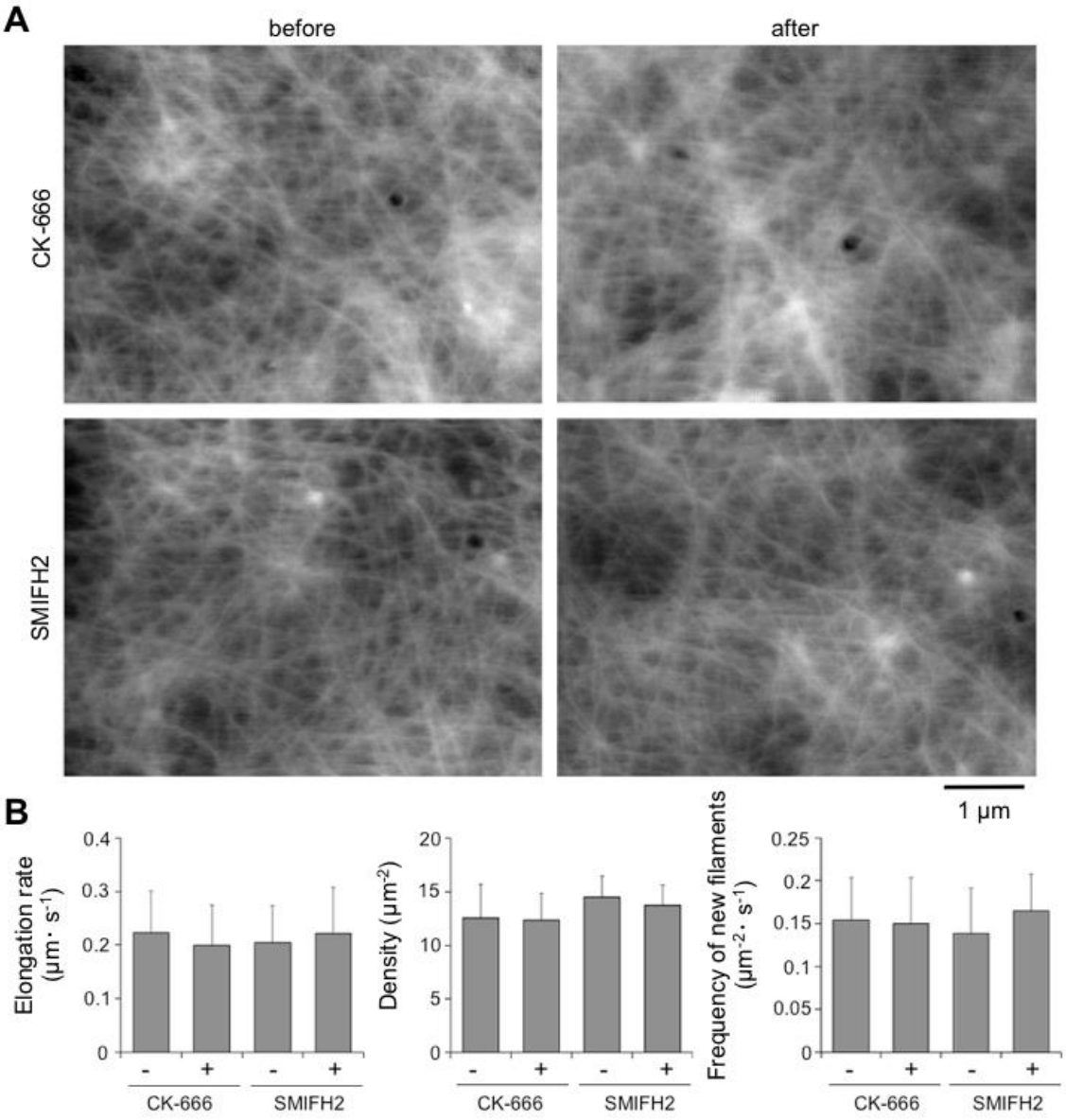

Fig 9. CK-666 and SMIFH2 didn't affect cortical actin dynamics

(A) AFM images of cortical actin dynamics before and after treatment with CK-666 and SMIFH2.

(B) Analysis of the frequency of newly assembled actin filaments, the density and the elongation rate of actin filaments of the cells treated with CK-666 and SMIFH2. Error bar indicates SD.

The effects of actin-binding proteins that control actin G-actin pool were also investigated. Profilin binds to G-actin and regulates the elongation at the barbed end, whereas thymosin β4 competes with profilin to sequester G-actin from being polymerized into filaments (Pantaloni and Carlier, 1993). EGFP-profilin or mCherry-thymosin β4 was overexpressed in COS-7 cells, and the actin filament turnover was visualized by HS-AFM and then analyzed. The fluorescence signal of EGFP and mCherry was observed by fluorescence microscope installed in the inverted microscope of the HS-AFM unit to confirm the expression of fluorescent-tagged proteins in the target cell. The analysis of cortical actin filaments revealed that these proteins had little effects on the elongation rate and the density of actin filaments **(Fig. 10)**. This is probably because the cytoplasmic G-actin pool is already saturated by the endogenous amounts of the G-actin bound proteins.

2.3.4 Descension of newly assembled filaments

The fate of a newly assembled actin filament was followed in the time-lapse observation of HS-AFM. The filaments gradually faded out and finally became invisible in 10-90 seconds after the assembly (**Fig. 11A**). The analysis of the vertical position of the filament revealed that the assembly mainly occurred near the plasma membrane, and that the newly assembled filament gradually descended into the interior of the cell (**Fig. 11B**).

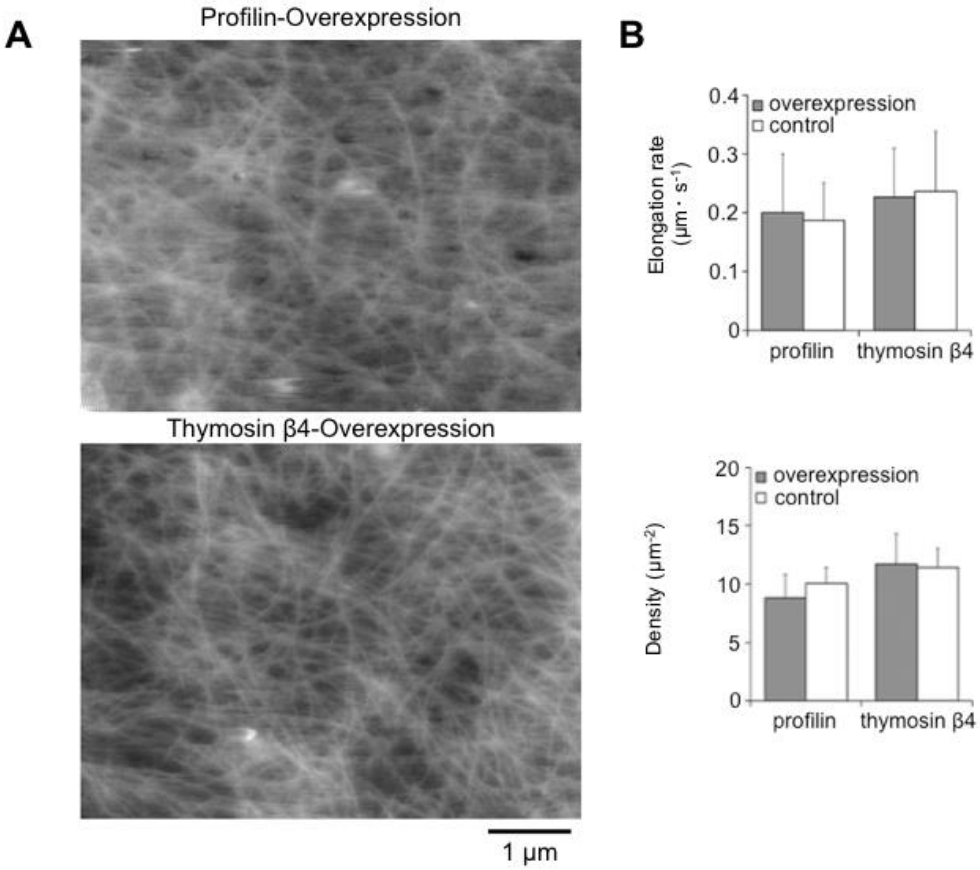

Fig 10. Overexpression of profilin and thymosin β4 didn't affect cortical actin dynamics

(A) AFM images of cortical actin dynamics in the cell over-expressing profilin or thymosin β4.

(B) Analysis of the density and the elongation rate of actin filaments of the control cells and cells over-expressing profilin or thymosin β4. Error bar indicates SD.

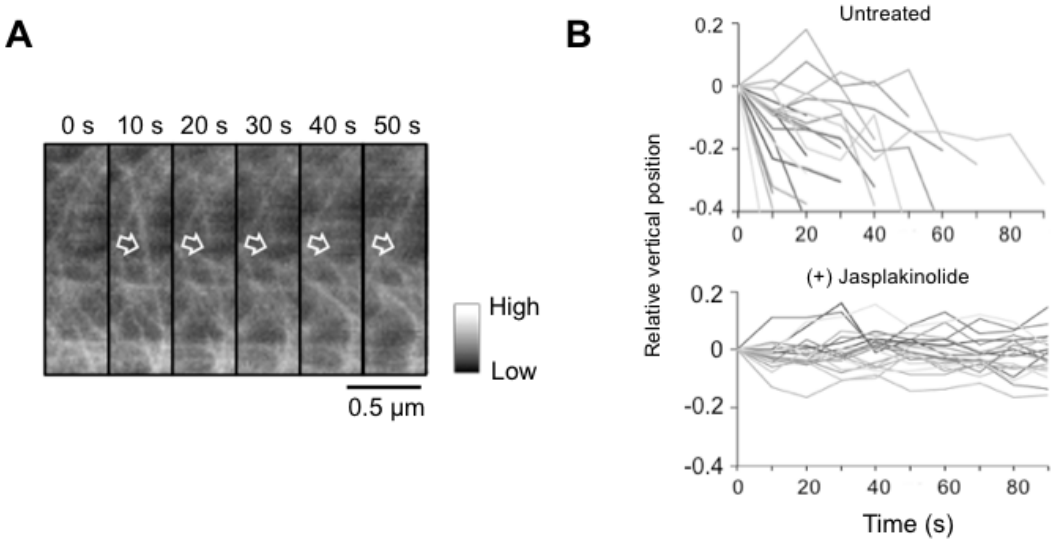

Fig 11. Descension of actin filaments

(A) The descension of an actin filament (arrow) after appearance. A new actin filament appeared between 0 and 10 seconds and gradually become invisible. The white area showed a higher position and the black area showed a lower position in the cell.

(B) The relative vertical position of 20 filaments when actin filament appeared and gradually disappeared was plotted. After treatment with jasplakinolide, the descension of newly appeared actin filaments stopped.

Interestingly, treatment with jasplakinolide almost completely stopped the descension **(Fig. 11B)**. This suggested that the descension of actin filaments is driven by new assembly of filaments near the plasma membrane.

The spatiotemporal resolutions of the HS-AFM did not allow to determine whether the disappearance of the filaments was due to descension outside the imaging depth or depolymerization. The depolymerizing end was rarely captured by HS-AFM. Considering the dissociation rate constants of F-actin *in vitro* (0.89 s^{-1} and 0.19 s^{-1} for the barbed and pointed ends, respectively) (Kuhn and Pollard, 2005) and the half time of cortical actin turnover (~20-45 s) reported previously (Murthy and Wadsworth, 2005; Fritzsche et al., 2013), it was possible that the actin depolymerization or severing occurred during the descension.

2.4 Discussion and conclusion

In this study, I established a method to visualize and analyze dynamics of cortical actin filaments in a living cell by using HS-AFM. This is the first observation of the dynamics of individual cortical actin filaments in a living cell with a second-order temporal resolution. The kinetic parameters obtained here (elongation rate, frequency of initiation, etc.) are different among different cell lines and also from the results obtained from other

biochemical approaches. There are several important issues to be discussed on such results.

2.4.1 Actin elongation rate in a living cell

Actin elongation was traced in living COS-7 cells with a rate of 0.19 ± 0.07 μm・s^{-1} (~70 subunits per second) at room temperature by HS-AFM. Although it was reported that two subpopulations with different polymerization rates existing in the cell cortex (Fritzsche et al., 2013), it was difficult to capture faster actin elongation by HS-AFM in an area of 6×4.5 μm^2 with the scanning speed of 0.1 frame per second. Referring to the estimation of the recent paper with two subpopulation rates of 1.3 μm・$s^{-1}$and 0.4 μm・s^{-1} respectively at cell cortex (Sakamoto et al., 2018), most of the actin filament elongation traced by HS-AFM may be the slower elongation of actin filaments. This may be due to the imaging at room temperature in my HS-AFM system.

2.4.2 Descension of the newly assembled filament from the surface into the cytoplasm

As shown in **Fig. 11**, the actin filaments were newly assembled near the plasma membrane and gradually descended into the interior of the cell, and never ascend towards the plasma membrane. These results suggest that polymerization mostly occurs near the plasma membrane, and imply the existence of a membrane-bound actin nucleator and/or

other regulatory factors. Addition of jasplakinolide inhibited the turnover of cortical actin, and also the descending movement of the filaments. At the same time, the duration that actin filament can be observed extended (90 s~) **(Fig. 11B)**, demonstrating that the descension of the filaments is driven by new filament assembly near the plasma membrane. The quantitative analysis showed actin filaments become invisible 10-90 seconds after assembly. Considering the half time of cortical actin turnover (~20-45 s) (Murthy and Wadsworth, 2005; Fritzsche et al., 2013), the possibility can't be denied that the actin depolymerization or severing occurred during the descension despite the fact that the depolymerization process was rarely captured by HS-AFM. Although the biological function of the actin filaments descension at cell cortex is still not understood, it may possibly involve in the process during endocytic vesicles entering into cells.

2.4.3 How the actin monomer pool is maintained in the cortex

Considering the importance of G-actin monomer to replenish the stock for actin polymerization and maintain the turnover of cellular actin, it is necessary to estimate the amount of the free G-actin in living cells. The observation that the addition of jasplakinolide immediately reduced not only the depolymerization but also polymerization rates **(Fig. 8)** suggests that a small amount of free G-actin pool is present in the cortex. The density of the filament was not significantly increased by the addition

of the inhibitor also demonstrating that free G-actin pool in the cytoplasm, or at least in the cortical layer of COS-7 cells is very low. For the reason that free G-actin concentration is proportional to the actin polymerization rate, the free G-actin pool was estimated from the elongation rate. The rate constant at barbed end was reported as 11.6 $\mu M^{-1}s^{-1}$ (Pollard, 1986) and a similar level of ~10 $\mu M^{-1}s^{-1}$ estimated by time-lapse observation of fluorescently labeled actin (Fujiwara et al., 2002). The free G-actin pool at cell cortex could be estimated as 6-7 μM. Considering the effect of *in vivo* factors which enhances actin polymerization such as profilin, the actual free G-actin pool may be far less than the estimated value at cell cortex, which is much lower than the total G-actin concentration in the cell (~100 μM). There could be several reasons for this discrepancy. First, a large free G-actin pool may exist in the cytoplasm, whereas the cell cortex has a small pool. Second, a large amount of G-actin exists in cells, but most of them are tightly regulated by various actin-binding proteins such as profilin, thymosin β4 or ADF/cofilin in living cells. This aligns well with the previous report that the free G-actin is far less than the profilin-bound or thymosin β4-bound G-actin (Kiuchi et al., 2011), and also explains the reason for my results why overexpression of profilin or thymosin β4 did not affect the turnover dynamics of cortical actin filaments **(Fig. 10)**.

A number of proteins are already known to regulate actin turnover such as those that bind to actin monomers (profilin, thymosin β4) and the others that bind to the filament (capping protein, Arp2/3 complex). The amount of these proteins, together with the activity of individual molecules, contributes to the maintenance of the G-actin pool. Profilin binds to actin monomers and competes with capping protein to facilitate actin elongation. Thymosin β4 also binds to actin monomers and blocks the actin assembly reactions. Although the dissociation constant of thymosin β4 to actin (K_D = 1-2 μM) is larger than that of profilin (K_D = 0.3-0.5 μM), a large amount thymosin β4 in the cytoplasm (100-500 μM) compared to that of profilin (10-80 μM) can sequester most of the free actin pool from polymerization (Yu et al., 1993; Carlier et al., 1993; Kang et al., 1999). It seems to be the case in COS-7 cells that a large amount of endogenous thymosin β4 and profilin maintain a low level of free G-actin pool in the cell cortex. Precise control of the expression level of these proteins in the target cell will clarify more detailed information about the free G-actin pool and cortical actin dynamics.

2.4.4 Different regulatory mechanisms in the cortex from lamellipodia

It is unexpected that proteins involved in the regulation and maintenance of actin dynamics in lamellipodia (formins and Arp2/3 complex) didn't show any effects on cell cortex **(Fig. 9)**. Formins promote the nucleation and elongation of actin filaments (Pruyne

et al., 2002). A formin inhibitor SMIFH2, which was previously demonstrated to affect the turnover rate of cortical actin (Fritzsche et al., 2013), did not change the polymerization rate, frequency of new assembled F-actin, or density of the filaments in the cortical layer of COS-7 cells observed by HS-AFM **(Fig. 9)**.

Similarly, an inhibitor of the Arp2/3 complex, CK-666, also did not change the dynamics of the cortical actin. The Arp2/3 complex binds to F-actin, and promotes actin nucleation at a 70° branch angle to the parent filament (Amann and Pollard, 2001). It plays critical roles in the formation of actin network at the leading edge of migrating cells (Lai et al., 2008). Due to the branching activity of Arp2/3 complex, lamellipodium has a number of barbed ends. They elongate towards the plasma membrane and generate a mechanical force to push the cell edge outward. In contrast to such orientation of actin ends at the lamellipodium, the cortical actin filaments run in parallel to the plasma membrane. The HS-AFM observation that the cortical actin dynamics was independent of Arp2/3 complex may be due to the reason that the branching activity of Arp2/3 complex is very low.

Previous studies using HeLa cells, M2 melanoma cells and primary cultured Sertoli cells demonstrated the involvement of Arp2/3 complex and formin in the formation of cortical action (Fritzsche et al., 2013, 2016; Sakamoto et al., 2018). This may partly due

to different regulatory mechanisms in different cell lines. As shown in **Figure 7**, the frequency of new assembled actin filaments varied in different cell types. Other membrane-bound protein such as ERM complex may play a role in the nucleation in COS-7 cells. The other possibility is that the concentration and specificities of the inhibitors. In this study, relatively low concentration of the inhibitor was used (10.6 μM for SMIFH2 and 50 μM for CK-666, respectively) compared to the previous studies (30-40 μM (SMIFH2) and 50-100 μM (CK-666)). Since SMIFH2 has different affinities to different formins, other types of formin might be working in the cortex of COS-7 cells. Further investigation is needed to clarify this issue.

2.4.5 Conclusion

In this chapter, I established a new microscopic approach to visualize and analyze cortical actin dynamics in a living cell by utilizing HS-AFM. This technique has several advantages over conventional microscopic techniques. First, it does not require any labeling, staining or overexpression of tagged protein, and still can dissolve individual actin filaments in a living cell. Second, it has high spatial and temporal resolutions to resolve the dynamics of actin filaments. Second-order temporal resolution and nanometer-order spatial resolution were proved to be enough to follow and analyze the dynamics of actin filaments in COS-7 cell. Third, AFM head mounted on the stage of an

inverted microscope enables a correlative imaging with fluorescence microscope. This provides a great potential for the integration with various fluorescence-based structural and functional imaging. Combining such HS-AFM technique with other various technical approaches will contribute for elucidating the molecular mechanism of how cortical actin is regulated.

Chapter 3

Molecular mechanism of how transcription co-regulator YAP controls cortical actin

3.1 Introduction

YAP (Yes-associated protein 1) is a transcription co-regulator that works with TEA domain family member (TEAD) transcription factors (Yagi et al., 1999; Kanai et al., 2000), and regulate many cellular events, such as cell proliferation, migration, and differentiation (For review Panciera et al., 2017). The activity of YAP is known to be controlled by several upstream factors which modulate its subcellular localization between nucleus and cytoplasm (Zhao et al., 2007; Dupont et al., 2011; Aragona et al., 2013). Mechanical stimulus is one of the most unique and well-studied mechanisms which regulate intracellular localization of YAP. So far, cell density (Zhao et al., 2007), the stiffness of ECM (Dupont et al., 2011) and lateral stretching (Aragona et al., 2013) have been demonstrated to control YAP localization. Actin and its related proteins are involved in mechano-sensing of YAP. The depletion of capping protein or cofilin increased stress fibers and facilitated the nuclear localization of YAP, while decreasing stress fibers by cytochalasin D inhibited the nuclear localization (Aragona et al., 2013; Wada et al., 2011; Dupont et al., 2011). When cell-cell contact increased, YAP localized in the cytoplasm, whereas actomyosin increased the nuclear localization of YAP (Das et al., 2016; Furukawa et al., 2017).

In addition to mechano-sensing pathway which changes the localization of YAP, a downstream pathway also controls intracellular actin structures, making a feedback signaling pathway. For example, in a gastric cancer cell line MKN28, YAP activates the expression of ARHGAP29, one of the Rho GTPase activating enzymes (RhoGAP), and the following signaling pathway (RhoA-ROCK-LIMK-cofilin pathway), which results in the depolymerization of F-actin and promotion of cell metastasis (Qiao et al., 2017). The linkage between YAP and ARHGAP29 has also been identified in endothelial colony-forming cells (ECFCs). YAP and its homologue TAZ inhibited RhoA-ROCK-MLCP pathway by regulating the expression of ARHGAP28, ARHGAP29 and NUAK2, which consequently control the cytoskeletal tension in ECFCs (Mason et al., 2019). YAP mutant fish (*hirame* (*hir*)) had a reduced level of ARHGAP18, reduced actomyosin tension, and a flattened body shape (Porazinski et al., 2015).

A number of studies mentioned above demonstrated a tight linkage between YAP and actin cytoskeleton and actin-regulatory proteins. The morphology of YAP-knockdown cells suggested that not only stress fibers, but also cortical actin, are under the control of YAP-regulating genes (Porazinski et al., 2015). However, the molecular mechanism of such downstream pathway has not been well understood. Considering such situation, here I decided to investigate the linkage between YAP activity and the structure of cortical

actin by utilizing the method of HS-AFM that I established in the previous chapter. HS-AFM imaging of the cell cortex, combined with other microscopic techniques and mechanical characterizations, will elucidate how cortical actin filaments are controlled by YAP-regulated genes.

3.2 Materials and methods

3.2.1 Cell culture

MDCK control, YAP-KO cells and RPE control, YAP-KO cells (a gift from Professor Seiki, Yamaguchi University) were cultured in Dulbecco's Modified Eagle's Medium (DMEM)-high glucose (Nacalai Tesque) supplemented with 10% fetal bovine serum (FBS). The cells were maintained in plastic culture dishes at 37 ℃ and 5% CO_2.

3.2.2 Plasmid and transfection

The plasmid of pmCherry-YAP1 was extracted from RPE cells by RNeasy kit (Qiagen) and reverse transcripted into cDNA by SuperScript^{TM} First-Strand Synthesis System (Invitrogen). Then the cDNA of YAP1 was amplified by 2-step PCR using the following primers:

1st-step Forward: TAGCCCTCGCTCGCCTGGGTCAGGGGGTGC;

Reverse: GGTGCATGTGTCTCCTTAGATCCTTCACAG;

2nd-step Forward: AAAGTCGACATGGATCCCGGGCAGCAGC;

Reverse: CGCGGTACCCTATAACCATGTAAGAAAGCT;

and inserted into KpnI and SalI sites of pmCherry-C1. The insertion was verified by DNA sequencing. The plasmid of pcDNA-3×FLAG ArhGAP18 was a gift from Professor Seiki of Yamaguchi University. Plasmids encoding constitutive active RhoA (RhoA(Q63L)) and E-cadherin were purchased from Cell Biolabs, Inc. and Addgene respectively. The plasmids were introduced into cells using Effectene Transfection Reagent (Qiagen) or PEI-MAX (Polysciences).

3.2.3 Fluorescence microscope

For phalloidin staining, cells were washed 3 times with cold phosphate-buffered saline (PBS) and then fixed with 4% paraformaldehyde (PFA) for 15 minutes. After washing 3 times with PBS, cells were permeabilized with 0.1% Triton X-100 in PBS for 15 minutes, and then incubated with 1:500 Rhodamine-Phalloidin (Cytoskeleton, Inc.) in PBS for 1 hour, followed by 3 times washes with PBS. At last, cells were counterstained with Hoechst33342 (Nacalai Tesque) for nuclei.

For ARHGAP18, RPE cells were washed 3 times with cold PBS and then fixed with 4% PFA for 15 minutes. After washing 3 times with PBS, cells were permeabilized and blocked with 0.1% Triton X-100 and 5% normal goat serum (NGS) in PBS for 15 minutes

followed by 3 times PBS washes, and then incubated with 1:500 anti-ARHGAP18 antibody (Rabbit, Abcam) in 5% NGS in PBS overnight at 4℃, followed by 3 times washes with PBS. Cell were then incubated with 1:500 Fluorescein (FITC)-conjugated goat anti-rabbit IgG antibody (Cappel) in 5% NGS in PBS or 1:500 FITC-conjugated goat anti-rabbit IgG antibody with 1:500 Rhodamine-Phalloidin (Cytoskeleton, Inc.) in 5% NGS in PBS for 1 hours. After washing 3 times with PBS, cells were counterstained with Hoechst33342 (Nacalai Tesque) for nuclei.

For E-cadherin overexpression experiment, RPE cells were transfected with the plasmid encoding EGFP-fused E-cadherin. After 24 hours, the cells were washed 3 times with cold PBS and then fixed with 4% PFA for 15 minutes. After washing 3 times with PBS, cells were permeabilized and blocked with 0.1% saponin and 5% NGS in PBS for 15 minutes followed by 3 times PBS washes, and then incubated with 1:500 anti-ARHGAP18 antibody (Rabbit, Abcam) in 0.1% saponin and 5% NGS in PBS overnight at 4℃, followed by 3 times washes with PBS. Cell were then incubated with 1:500 Texas Red-conjugated goat anti-rabbit IgG antibody (Molecular probes) in 0.1% saponin and 5% NGS in PBS for 1 hours. After washing 3 times with PBS, cells were counterstained with Hoechst33342 (Nacalai Tesque) for nuclei.

Z-stack Images were taken by a confocal microscope FV3000 (Olympus) with a PlanApo 60× (1.42 NA) oil immersion objective.

3.2.4 Western blot

Cell lysate was prepared from RPE cells at 40% confluency. After washing with PBS for 3 times, the cells were dissolved in 5% SDS in Milli-Q with pipetting using syringe and incubated for 20 minutes at room temperature. The proteins were separated in polyacrylamide gels by SDS-PAGE and then transferred into PVDF blotting membrane (GE healthcare Life Science) by semi-dry or wet tank transfer system. And then membranes were blocked in 5% skim milk blocking solution in TBST buffer for 1 hour at room temperature. Membranes were incubated with 1:1000 anti-ARHGAP18 primary antibody (Rabbit, Abcam) or anti-α-tubulin primary antibody (Mouse, Sigma) in TBST buffer overnight at 4 ℃. After washing with TBST buffer for 3 times, membranes were incubated with 1:5000 HRP-conjugated anti-rabbit, or anti-mouse IgG (H+L) secondary antibody (Invitrogen) in TBST buffer for 1 hour at room temperature. Signals were detected with Chemi-Lumi One Super (Nacalai Tesque) or Chemi-Lumi One L (Nacalai Tesque) and images were taken by LAS-3000 mini (Fujifilm).

3.2.5 AFM force measurement

MDCK cells (control and YAP-KO) were seeded on a 50 mm diameter glass bottom dish with the glass diameter of 40 mm (FluoroDish^{TM}) at a sparse density one day before measurement and kept at 37 ℃ and 5% CO_2. New DMEM-high glucose culture medium was changed and 1:100 HEPES solution (Sigma) was added into the medium 30 minutes before measurement.

After setup of a silicon cantilever with a 5 μm ± 10% colloidal particle (CP-CONT-BSG, sQube), the AFM scanning head (MFP-3D, Asylum Research) was placed on an inverted microscope (IX71, Olympus) stage. The stage was maintained at 37 ℃. Spring constants ranged from 0.02 to 0.77 N/m and the values of each cantilever were determined by a thermal method. Cortex of each cell was chosen as a target.

Data was processed by SPIP^{TM} (Image Metrology). Force curves were fitted by Hertz-fit ranged from 0 to 10 nN. 20 pushes were continued to calculate the average force and at least 52 cells were measured.

3.2.6 Protein purification

rGBD-pGEX-6P-1, pGBD-pGEX-6P-1, wGBD-pGEX-6P-1 were expressed in RIL cells as GST (Glutathione S-transferase) fusion proteins and then grown overnight in LB medium for pre-culture. Pre-culture was transferred to culture medium and continued

incubation. 1 mM IPTG was added to induce expression. And cells were incubated at 20 ℃, 120 rpm for overnight. Cells were harvested by centrifuge at 3000 g, 10 minutes, 4 ℃ and re-suspended with binding buffer (400 mM NaCl, 0.2 mM DTT in PBS), then quick froze by liquid nitrogen and thaw with warm water and repeated for 3 times. After adding 0.2 mg/mL lysozyme, 20 μg/mL DNase, 1 mM $MgCl_2$, 1 mM PMSF, cell lysates were incubated at room temperature for 30 minutes and centrifuged at 12,000 g, 15 minutes, 4 ℃. Supernatants were incubated with Glutathione-sepharose™ beads (GE Healthcare Bio-Science) at 4 ℃ for 2 hours. After incubation, the supernatants were thrown and the beads were washed with binding buffer for 3 times and eluted by 50 mM Glutathione binding buffer (pH 8.0), followed by dialysis overnight with 50 mM HEPES, 100 mM NaCl, 1 mM 2-mercaptoethanol. For rGBD-GST, the purified proteins were concentrated by Amicon® Ultra Centrifugal Filters (Ultracel®-3 K, 0.5 mL) at last. The concentrations of purified proteins were detected and calculated by CBB staining.

3.2.7 Pull down assay

RPE cells were seeded at a sparse density and transfected with pcDNA-3×FLAG ArhGAP18 if needed before 24 hours.

The cells were washed with cold PBS once and pull-down buffer (50 mM HEPES pH 7.4, 100 mM NaCl, 0.2 mM DTT) once and then collected with pull-down buffer with

1:100 protease inhibitor cocktail (Nacalai Tesque). After centrifugation at 500 g, 5 minutes, 4 ℃, cells were re-suspended with pull-down buffer with 1:100 protease inhibitor cocktail (Nacalai Tesque), 0.1% Triton-100 X and incubated on ice for 15 minutes. And then cell lysates were centrifuged at 10,000 g, 1 minutes, 4 ℃. 10 μg of these cell lysates were saved as loading controls. The left cell lysates were mixed with Glutathione-sepharose™ beads (GE Healthcare Bio-Science) and rGBD-GST, or pGBD-GST, or wGBD-GST, and incubated at a rotator at 4 ℃ for 2 hours. After the incubation, beads were washed by pull-down buffer once and eluted by 100 mM Glutathione pull-down buffer (pH 8.0) and detected by Western blot. The proteins were separated in 12% polyacrylamide gels by SDS-PAGE and then transferred into PVDF blotting membrane (GE healthcare Life Science) by wet tank transfer system.

For RhoA, membranes were incubated with 1:1000 anti-RhoA primary antibody (Mouse, Cytoskeleton, Inc.) in TBST buffer overnight at 4 ℃, and 1:5000 HRP-conjugated anti-mouse IgG (H+L) secondary antibody (Invitrogen) in TBST buffer for 1 hour at room temperature.

For Rac, membranes were incubated with 1:1000 anti-Rac primary antibody (Mouse, GeneTex) in TBST buffer overnight at 4 ℃, and 1:5000 HRP-conjugated anti-mouse IgG (H+L) secondary antibody (Invitrogen) in TBST buffer for 1 hour at room temperature.

For Cdc42, membranes were incubated with 1:1000 anti-Cdc42 primary antibody (Mouse, Cytoskeleton, Inc.) in TBST buffer overnight at 4 ℃, and 1:5000 HRP-conjugated anti-mouse IgG (H+L) secondary antibody (Invitrogen) in TBST buffer for 1 hour at room temperature.

For GAPDH, membranes were incubated with 1:5000 anti-GAPDH primary antibody (Rabbit, GeneTex) in TBST buffer overnight at 4 ℃, and 1:5000 HRP-conjugated anti-rabbit IgG (H+L) secondary antibody (Invitrogen) in TBST buffer for 1 hour at room temperature. For flag-tagged ARHGAP18, membranes were incubated with 1:1000 anti-FLAG primary antibody (Mouse, Sigma) in TBST buffer overnight at 4 ℃, and 1:5000 HRP-conjugated anti-mouse IgG (H+L) secondary antibody (Invitrogen) in TBST buffer for 1 hour at room temperature.

Signals were detected with Chemi-Lumi One Super (Nacalai Tesque) or Chemi-Lumi One L (Nacalai Tesque) and images were taken by LAS-3000 mini (Fujifilm).

3.2.8 Wound healing assay

MDCK cells (control, YAP-KO) were seeded on glass bottom dishes and incubated in DMEM-high glucose (Nacalai Tesque) supplemented with 10% FBS at 37 ℃ and 5% CO_2. The cells were scratched when they reached confluence and the medium was changed to DMEM-low glucose (Sigma) with 10% FBS, without phenol red. Images were

taken by FV3000 (Olympus) confocal laser scanning microscope with a UPLSAPO 10× (0.4 NA) objective. Scratch after 0 hour, 6 hours, 18 hours were recorded. At least 5 different wound sites were imaged and data was analyzed by ImageJ software (NIH).

3.2.9 Cell migration assay

MDCK cells were seeded on a glass bottom dish in a sparse density 24 hours before observation. Time-lapse images were taken by FV3000 (Olympus) confocal laser scanning microscope with a UPLSAPO 10× (0.4 NA) objective. DIC Images were taken 5 minutes per frame for total 3 hours. 20 areas were tracked for both control and YAP-KO cells.

3.2.10 Cell membrane photo-damage and live-cell imaging

Cells were seeded on glass bottom dishes at a sparse density and transfected with eGFP-N1 or pcDNA3-GFP-RhoA-Q63L. After transfection, cells were incubated for 24 hours in DMEM-high glucose (Nacalai Tesque) supplemented with 10% FBS at 37 ℃ and 5% CO_2.

Cell medium was changed to DMEM-low glucose (Sigma) with 10% FBS, without phenol red and 160 μg/mL Propidium Iodide (Sigma) was added into the medium 10 minutes before observation. Photo-damage and time-lapse imaging was performed by

FV3000 (Olympus) confocal laser scanning microscope with a UPLSAPO 100× (1.4 NA) oil immersion objective. Protocol was modified based on a previous study Jimenez et al., 2014. In brief, incubation chamber for live-cell imaging was stabilized at 37 ℃ and 5% CO_2. Time-lapse images were acquired every 30 seconds per frame. 3 frames were taken before laser damage for data analysis. UV-laser induced photo-damage was performed by a 405 nm ultraviolet laser with 10% of laser power in a 3 μm-diameter circle for 5 seconds. Cell morphology was confirmed by eGFP fluorescent signals and cell cortex was chosen as the target. Intensity curves were fitted with the following equation (Jimenez et al., 2014), $F(t) = \frac{Reff}{v} \cdot (1 - e^{-vt})$, where R_{eff} is the effective radius of the UV-laser induced hole, v is the closure rate of it.

All curve fittings were performed by ImageJ software (NIH). And the distributions of 2 data sets were compared by two-sample Kolmogorov-Smirnov test.

3.2.11 HS-AFM

A tip-scan high-speed atomic force microscope (HS-AFM) unit combined with an inverted fluorescent/optical microscope (IX83, Olympus) system (Suzuki et al., 2013) was used. The imaging technique of actin dynamics was developed based on the previous studies (Suzuki et al., 2013; Yoshida et al., 2015). A sharp cantilever tip with a spring constant of 0.1 N/m (USC-F0.8-k0.1-T12-10, Nanoworld) was used. Cells were seeded

on a slide glass coating with Poly-L-lysine (PLL) (Sigma). A specific area was chosen as a target based on the phase-contrast image of the cell. AFM images were taken every 10 seconds per frame. AFM images were exported to 320×240 pixels^2, and the scan area was 6×4.5 μm^2.

For RhoA Q63L overexpression experiments, MDCK cells were transfected with eGFP-N1 or pcDNA3-GFP-RhoA-Q63L more than 36 hours before observation. After transfection, cells were incubated in DMEM-high glucose (Nacalai Tesque) supplemented with 10% FBS at 37 ℃ and 5% CO_2. Fluorescent signals were confirmed by FV1200 (Olympus) confocal laser scanning microscope.

For image analysis, images were analyzed by ImageJ (NIH) software. For actin filament density and new assembled filaments analysis, 15 areas were randomly chosen in each movie per cell, and the area size was of 1×1 μm^2.

3.2.12 Image analysis and statistics

Image analysis was processed by ImageJ software or Fiji.

For stress fiber organization, an ImageJ software (NIH) plugin Fibriltool was used (Boudaoud et al., 2014). Z-projection images of Rhodamine-phalloidin staining were analyzed. A whole single cell was chosen as a ROI region. For cell migration, a Fiji plugin

Trackmate (Tinevez et al., 2016) was used to track the moving of a single cell automatically.

Statistical analysis was performed by Microsoft Excel software. F-test was performed to test if the variances of 2 populations were equal. And then based on the results of F-test, a 2-tailed, unpaired, t-test was performed to compare if the difference of 2 data sets is significant or not. *, $p<0.05$, **, $p<0.01$, ***, $p<0.001$.

3.3 Results

3.3.1 Characterization of actin distribution in YAP-knockout cells

3.3.1.1 YAP-KO cells have denser cortical actin filaments

The intracellular distribution of actin was first compared in normal cells and YAP-knockout cells. Madin-Darby canine kidney (MDCK) cell which was an epithelial cell line derived from the kidney of a normal adult dog in 1958 (Gaush et al., 1966), and retinal pigment epithelial (RPE) cell which is an epithelial cell line derived from the hTERT-transfected RPE-340 cell line (Rambhatla et al., 2002) were used in this study. The YAP-knockout cell lines of these cells were kindly provided by Professor Seiki at Yamaguchi University.

The structure of the cortical actin was firstly examined. The cortical actin filaments were visualized and analyzed in MDCK cells by HS-AFM established in the previous

part. The cortical actin dynamics of both control and YAP-KO MDCK cells was then analyzed. The density of actin filaments in YAP-KO cells (10.54 ± 1.80 μm^{-2}) was higher than the control cells (9.50 ± 1.29 μm^{-2}) (**Fig. 12A, 12B**). The frequency of newly appeared filaments was also higher in YAP-KO cells (2.87 ± 1.22 $\mu m^{-2} \cdot 10\ s^{-1}$) than control cells (2.45 ± 1.15 $\mu m^{-2} \cdot 10\ s^{-1}$) (**Fig. 12B**).

The stiffness of the cell cortex was characterized by Young's modulus by force measurement of AFM to confirm the results visualized by HS-AFM. YAP-KO cells showed significantly larger Young's modulus, meaning that it is stiffer than the control cells (**Fig. 13**). These results indicated that the cortical actin in YAP-KO cells is denser than that in the control cells.

3.3.1.2 Depletion of YAP increased the resistance of the cell cortex

The cortical actin layer in YAP-KO cells was further characterized by introducing a small membrane damage by strong focused laser irradiation (Jimenez et al., 2014), and the recovery of the membrane lesion was monitored by time-lapse microscopy. The membrane lesion was monitored by membrane-impermeable nucleic acid dye Propidium Iodide (PI).

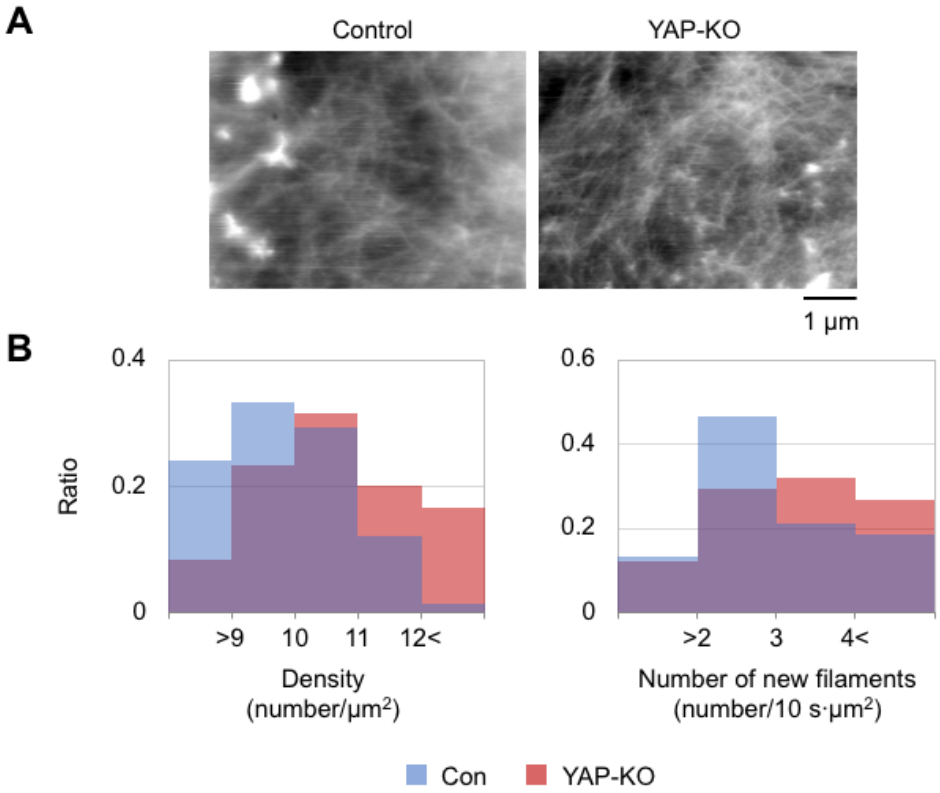

Fig 12. Visualization and analysis of cortical actin dynamics by HS-AFM showed a denser cortical actin in YAP-KO MDCK cells

(A) Representative cortical actin meshwork of control (left) and YAP-KO (right) MDCK cells visualized by HS-AFM. The scan area was 6 × 4.5 μm^2.

(B) Distributions of cortical actin filament density and number of newly assembled filaments were showed. For density analysis, N=5 cells, 75 areas for control group, N=4 cells, 60 areas for YAP-KO group. P-value<0.001, Student's t-test. For number of new filaments analysis, N=5 cells, 75 areas for control group, N=5 cells, 75 areas for YAP-KO group. P-value<0.05, Student's t-test.

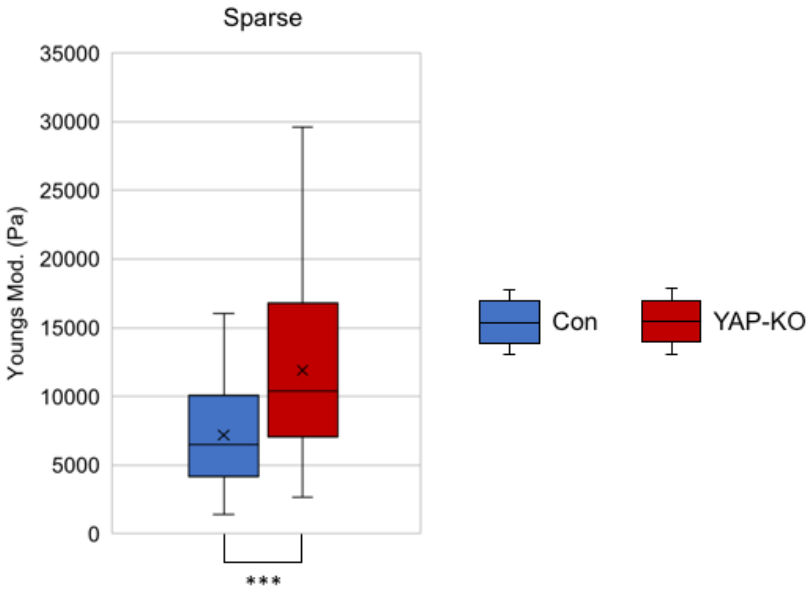

Fig 13. The stiffness of cell cortex measured by AFM showed stiffer cortex in YAP-KO cells
The data showed that the cortex of YAP-KO MDCK cells were stiffer than control MDCK cells. Error bar ± SD. N=52 cells for control group, N=56 cells for YAP-KO group. Cross means the average value. ***, $p<0.001$, Student's t-test.

Before performing the photo-damage on control and YAP-KO cells, the condition of laser irradiation was optimized. First, to determine the best duration for laser irradiation, 3 s, 5 s, 7 s, and 10 s in a 3 μm-diameter circle were examined. The results showed that with the increase of laser duration, more PI entered into the cells (**Fig. 14**). But when duration was increased to 10 s, the photo-damage was too strong and the cell died (data not shown). Then the photo-damage with different irradiation areas (1, 2, and 3 μm-diameter circle for 5 s) was examined. PI intensity was similar to each other under 3 μm diameter but decreased when the circular diameter increased to 6 μm (**Fig. 15**). From these results, the laser irradiation was decided to be 3 μm-diameter circle for a duration of 5 seconds.

Photo-damage and recovery was performed on control and YAP-KO MDCK cells. YAP-KO cells showed smaller amount of PI entry than control cells and reached to a lower plateau value in 1260 seconds after the damage (**Fig. 16**). To examine whether the different kinetics of the PI entry is due to the difference in the initial size of the lesion or the recovery rate, the curves of PI intensity was fitted to a formula reported in the previous research (Jimenez et al., 2014), $F(t) = \frac{Reff}{v} \cdot (1 - e^{-vt})$, where R_{eff} is the effective radius of the laser induced lesion, and v is the closure rate.

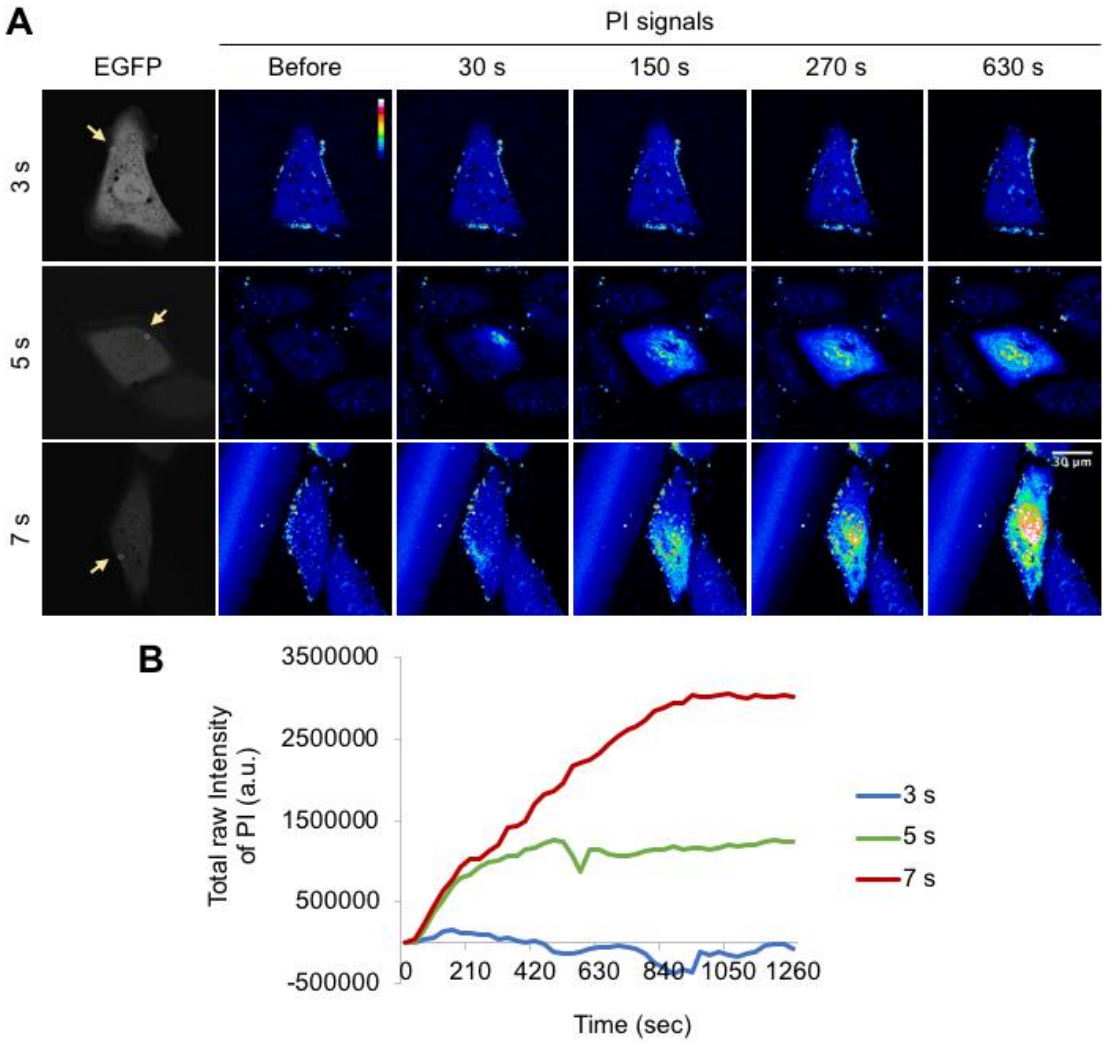

Fig 14. Photo-damage with different laser duration

(A) Time-lapse images of the photo-damage with 3 s, 5 s, 7 s laser duration. The first image (left) shows the cell morphology with EGFP signals. Laser was performed on the yellow circles with arrows. The PI intensity was shown by color bar with the time point before laser damage, 30 s, 150 s, 270 s, 630 s after laser damage.

(B) Representative intensity change of PI with time after 3 s, 5 s, 7 s 3 μm-diameter laser damage. The total analyzing time was 1260 s.

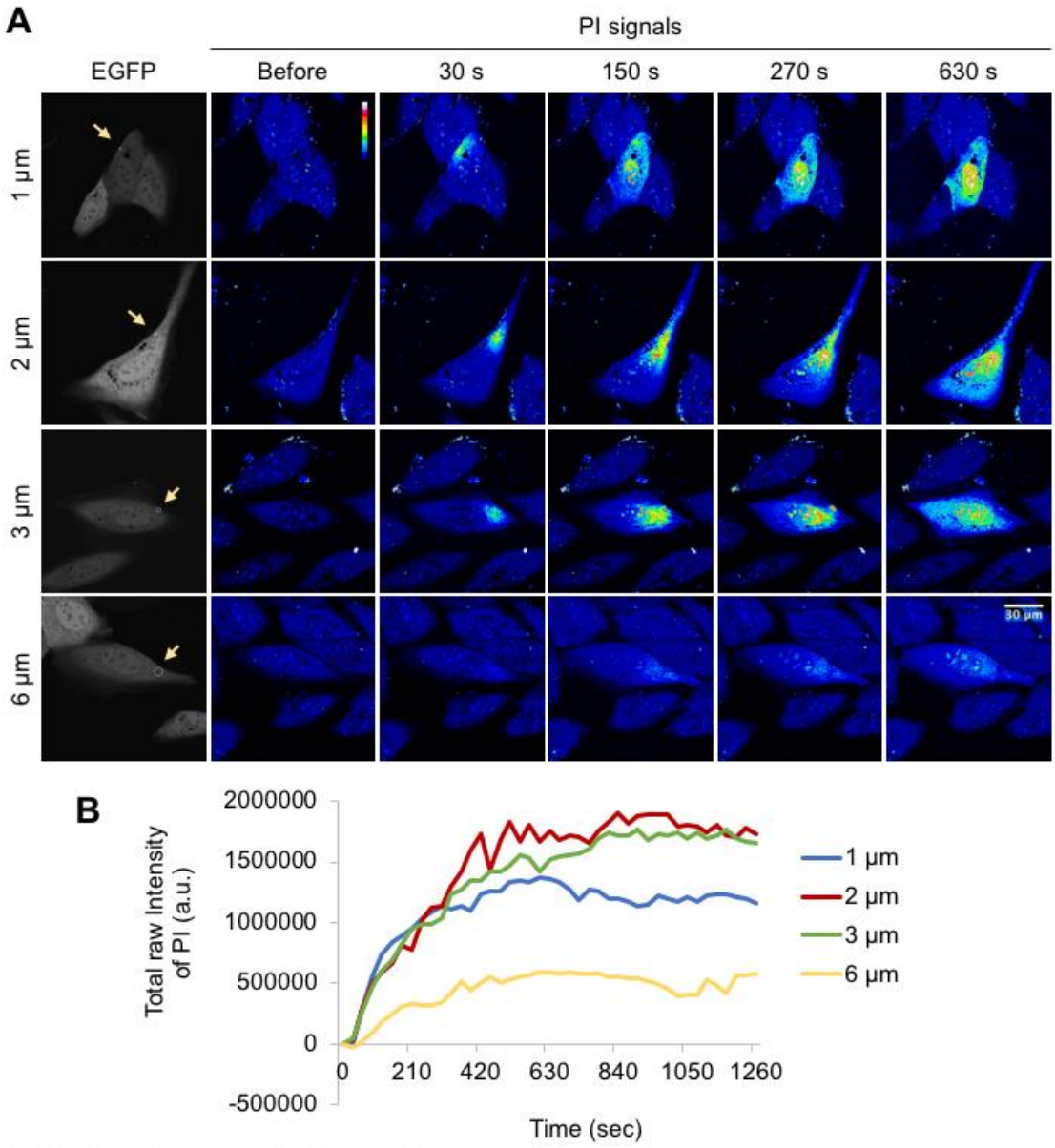

Fig 15. Photo-damage with different laser area

(A) Time-lapse images of the photo-damage with a laser area of 1 μm, 2 μm, 3 μm, 6 μm diameter. The first image (left) shows the cell morphology with EGFP signals. Laser was performed on the yellow circles with arrows. The PI intensity was shown by color bar with the time point before laser damage, 30 s, 150 s, 270 s, 630 s after laser damage.

(B) Representative intensity change of PI with time after 1 μm, 2 μm, 3 μm, 6 μm diameter for 5 s laser damage. The total analyzing time was 1260 s.

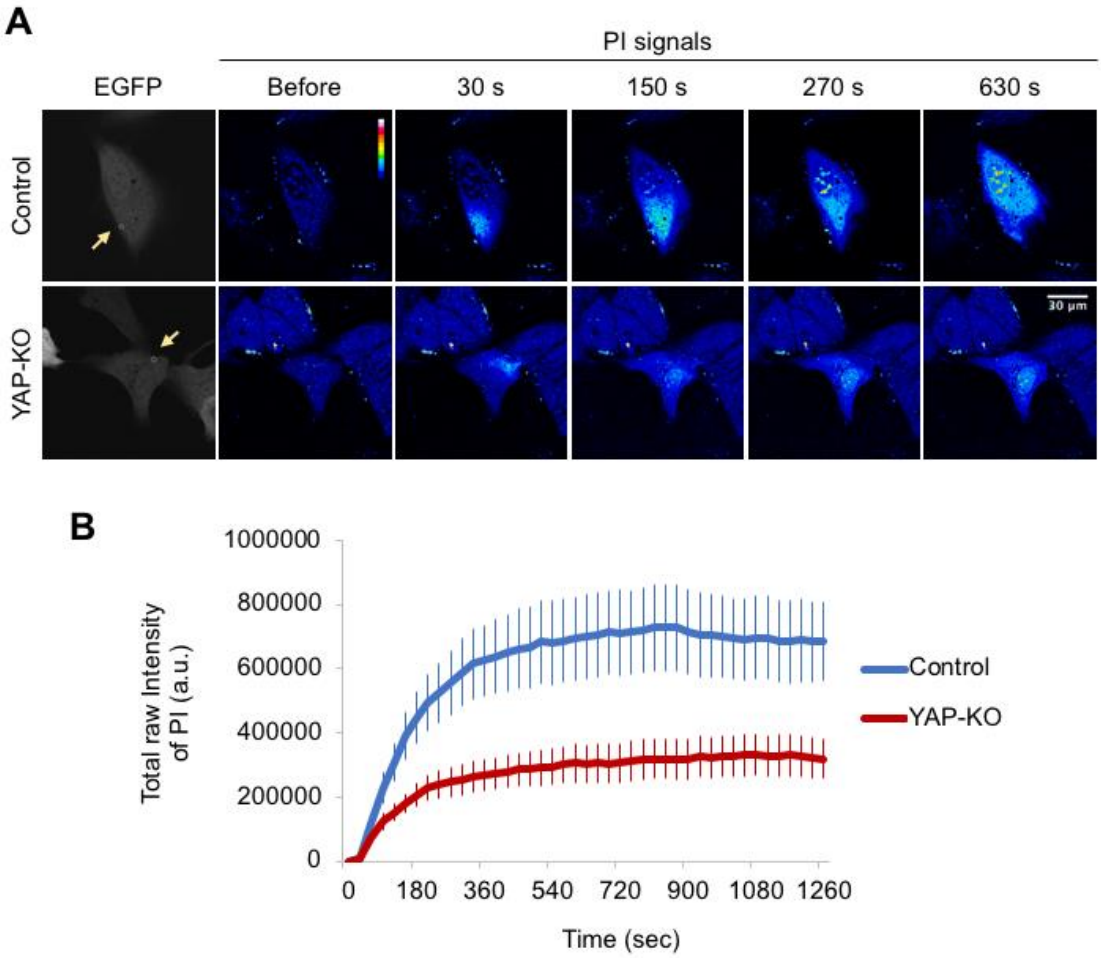

Fig 16. Photo-damage recovery of MDCK cells revealed increased resistance of cell cortex in YAP-KO cells

(A) Time-lapse images of the photo-damage performed on MDCK control (upper) and YAP-KO (down) cells. The first image (left) shows the cell morphology with EGFP signals. Laser was performed on the yellow circles with arrows. The PI intensity was shown by color bar with the time point before laser damage, 30 s, 150 s, 270 s, 630 s after laser damage.

(B) The intensity change of PI with time. The total analyzing time was 1260 s. Error bar ± 95% Confidence Intervals. N=44 cells for control group, N=40 cells for YAP-KO group.

The relationship between the effective radius and the closure rate was plotted (**Fig. 17A**). The distribution of closure rate had no significant difference between control and KO cells, whereas the effective radius was smaller in YAP-KO cells than control cells (**Fig. 17B, 17C**). The same analysis was performed in RPE cells (**Fig. 18**). Although PI entry showed a similar curve to MDCK cells (**Fig. 18B**), the detailed analysis of the effective radius and closure rate showed no significant differences between control and YAP-KO RPE cells (**Fig. 19**). These results indicated that the YAP-KO MDCK cells has stiffer cortical actin layer which is more resistant to an external damage, although RPE cells do not have significant differences.

3.3.1.3 Depletion of YAP did not affect stress fibers

MDCK cells were then stained with Rhodamine-phalloidin to visualize the stress fibers in the cells (**Fig. 20**). Phalloidin is a short peptide isolated from mushroom *Amanita phalloides* and has a high affinity to F-actin (Wulf et al., 1979). Control and YAP-KO MDCK cells showed similar distribution of stress fibers (**Fig. 20A**). The anisotropy of the stress fibers was also analyzed by an ImageJ plugin FibrilTool. Anisotropy was identified as the circular variance of the filamentous directions to describe if actin filaments were well ordered or not (Boudaoud et al., 2014). Quantification result showed YAP-KO cells had no significant difference with control cells (**Fig. 20B**).

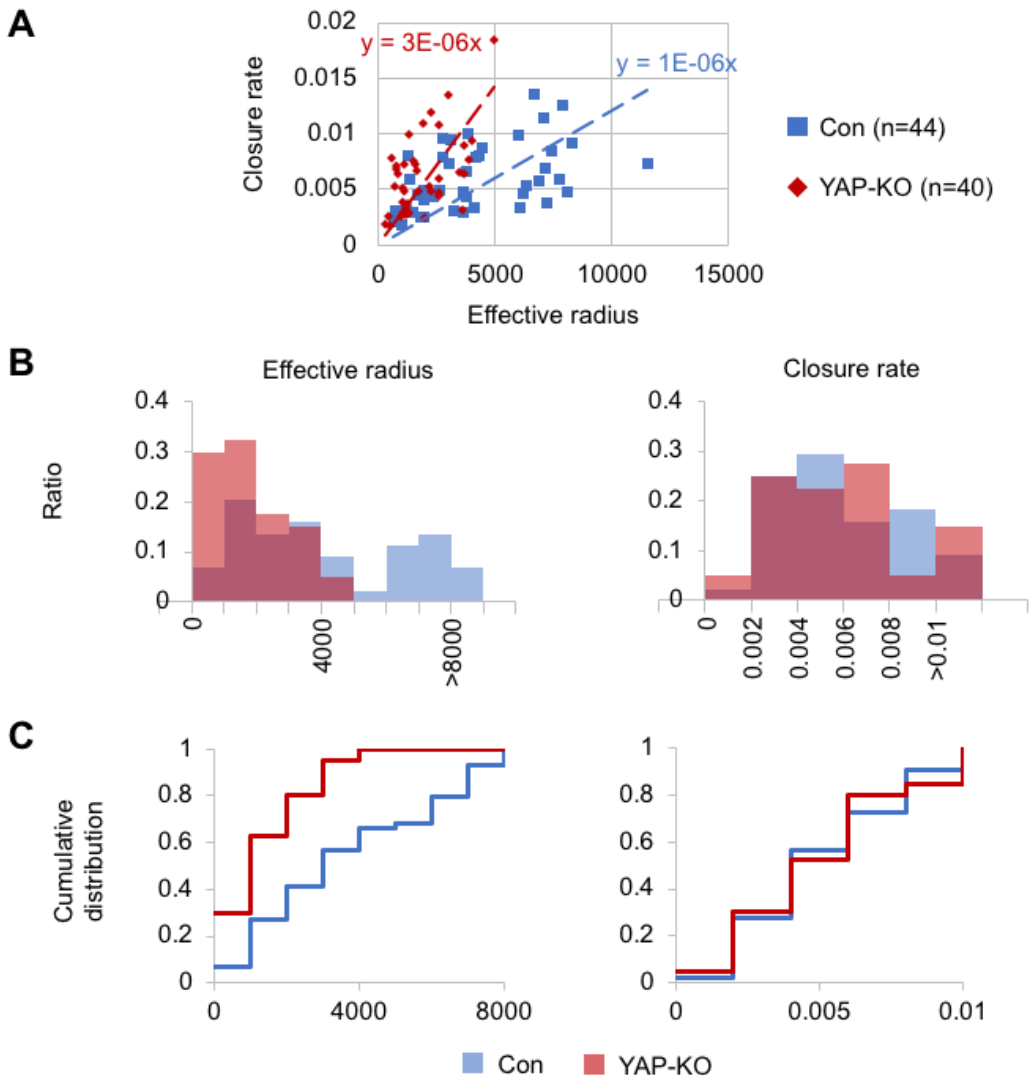

Fig 17. Analysis of MDCK PI fluorescence curves

(A) The PI fluorescence curve was fitted to a mathematical formula. Plot shows the closure rate and effective radius of laser-induced wounds. A liner approximation was fitted to explain the relation between the two factors in both control and YAP-KO cells.

(B) The distribution of the effective radius (left) and closure rate (right) of laser-induced wounds.

(C) Significance test of the distribution of effective radius and closure rate was taken by two-sample Kolmogorov-Smirnov test and the graph shows the cumulative distribution of effective radius (left) and closure rate (right). YAP-KO cells showed a significant decrease in effective radius of the wounds compared to control cells.

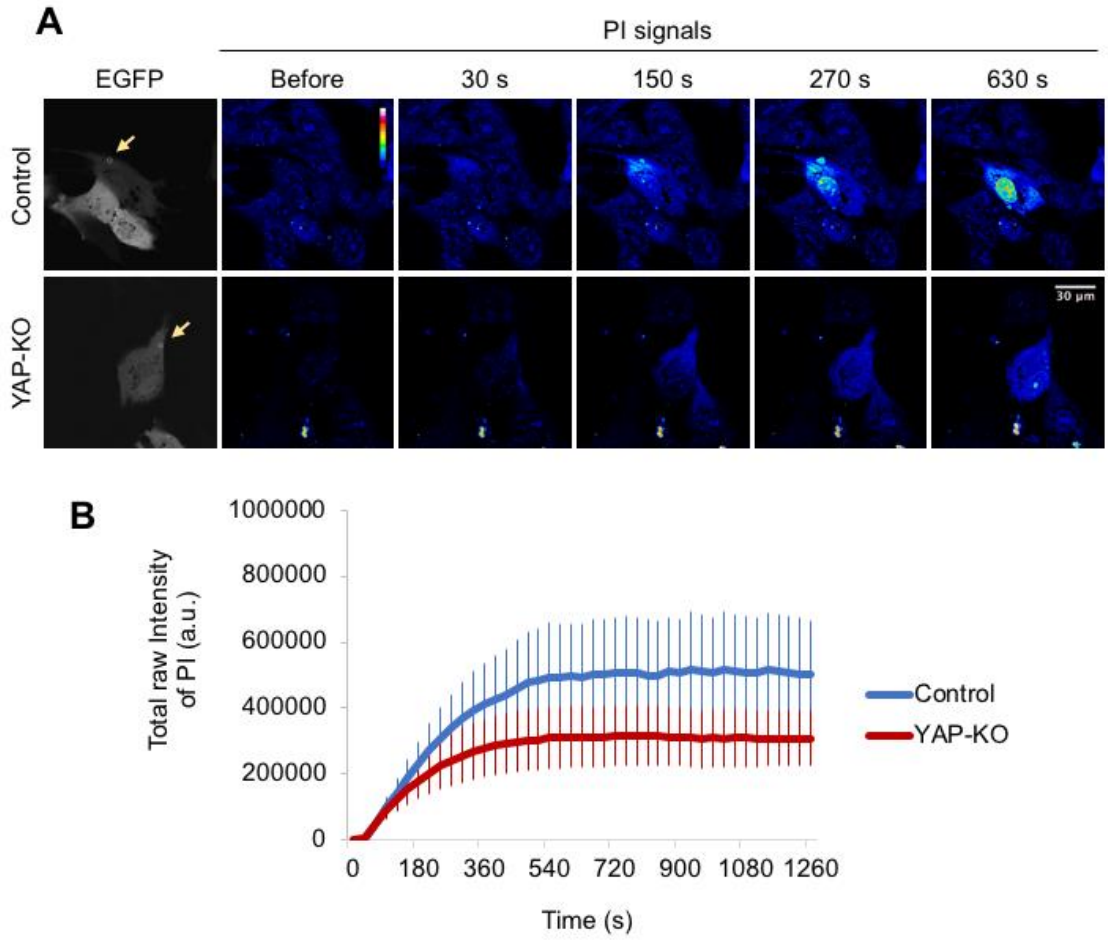

Fig 18. Photo-damage recovery of RPE cells showed a similar tendency as MDCK cells

(A) Time-lapse images of the photo-damage performed on RPE control (upper) and YAP-KO (down) cells. The first image (left) shows the cell morphology with EGFP signals. Laser was performed on the yellow circles with arrows. The PI intensity was shown by color bar with the time point before laser damage, 30 s, 150 s, 270 s, 630 s after laser damage.

(B) The intensity change of PI with time. The total analyzing time was 1260 s. Error bar ± 95% Confidence Intervals. N=28 cells for control group, N=31 cells for YAP-KO group.

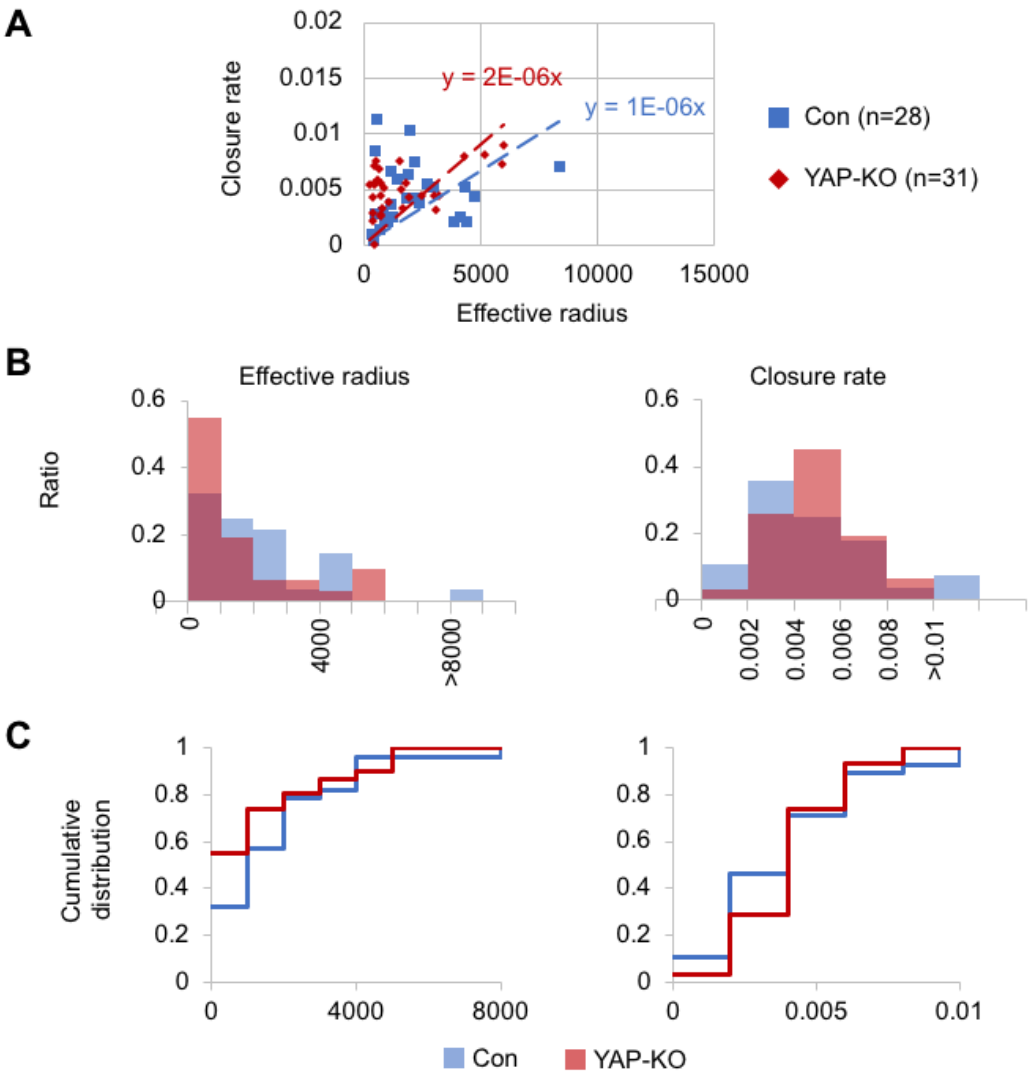

Fig 19. Analysis of RPE PI fluorescence curves

(A) The PI fluorescence curve was fitted to a mathematical formula. Plot shows the closure rate and effective radius of laser-induced wounds. A liner approximation was fitted to explain the relation between the two factors in both control and YAP-KO cells.

(B) The distribution of the effective radius (left) and closure rate (right) of laser-induced wounds.

(C) Significance test of the distribution of effective radius and closure rate was taken by two-sample Kolmogorov-Smirnov test and the graph shows the cumulative distribution of effective radius (left) and closure rate (right). Not significant differences for both effective radius and closure rate.

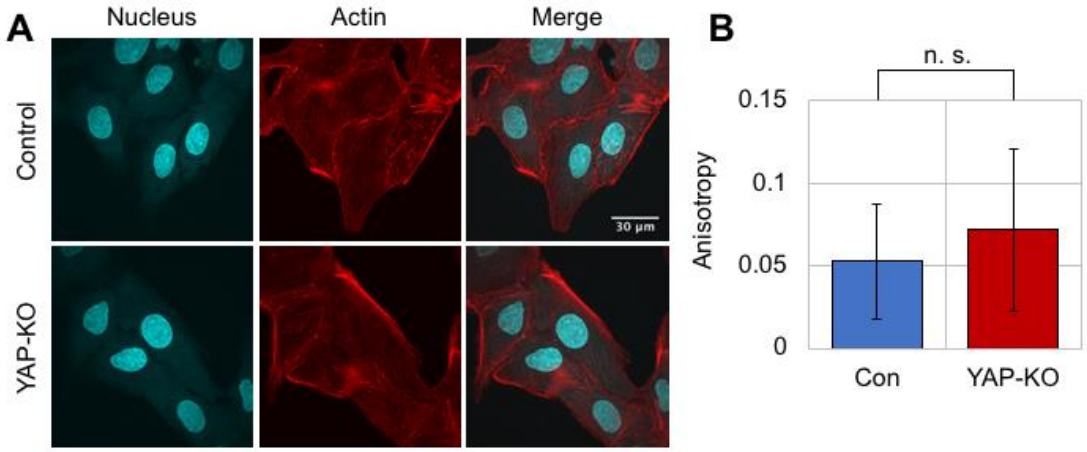

Fig 20. Stress fibers of MDCK cells stained with Rhodamine-Phalloidin didn't have significant differences between control and YAP-KO cells

(A) Control (upper) and YAP-KO (down) MDCK cells stained with Rhodamine-Phalloidin. Nucleus was stained with Hoechst33342.

(B) Analysis of actin filamentous anisotropy to determine if the filaments were well ordered or not. Error bar ± SD. N=25 cells for control group, N=22 cells for YAP-KO group. n.s., not significant, Student's t-test.

3.3.1.4 YAP-KO cells migrate slower than control cells

Control and YAP-KO MDCK cells were seeded at a sparse density on a glass bottom dish and the cell movement was tracked by differential interference contrast (DIC) microscopy. In a total observation time of 3 hours, YAP-KO cells showed a decrease in moving speed comparing with the control cells, although both of them showed a similar directionality (**Fig. 21A, 21B**). The cell motility was also analyzed by wound-healing assay, in which a confluent layer of cells was scratched and the recovery of the cell gap was followed by DIC imaging. Images were taken at 0, 6 and 18 hours after the scratching, and the area of the gap was quantified. YAP-KO MDCK cells showed a slower recovery than control MDCK cells (**Fig. 21C, 21D**), demonstrating a slower migration of KO cells.

The reduced motility of YAP-KO cells suggested that the dynamics of lamellipodia has been affected by YAP-KO. To investigate this possibility, the lamellipodia of YAP-KO cells were observed by HS-AFM, and the dynamics of the cell-edge (extension/retraction cycle) was analyzed (**Fig. 22A**). The position of the cell edge and the height were quantified and plotted against time (**Fig. 22B**). The height increased when the cell membrane moved forward, meaning that more actin polymerize. This is in good agreement to the previous research showing a correlation between the leading edge velocity and the intensity of LifeAct in lamellipodia (Ryan et al., 2012). When these dynamics was compared with control and YAP-KO cells, no significant difference could

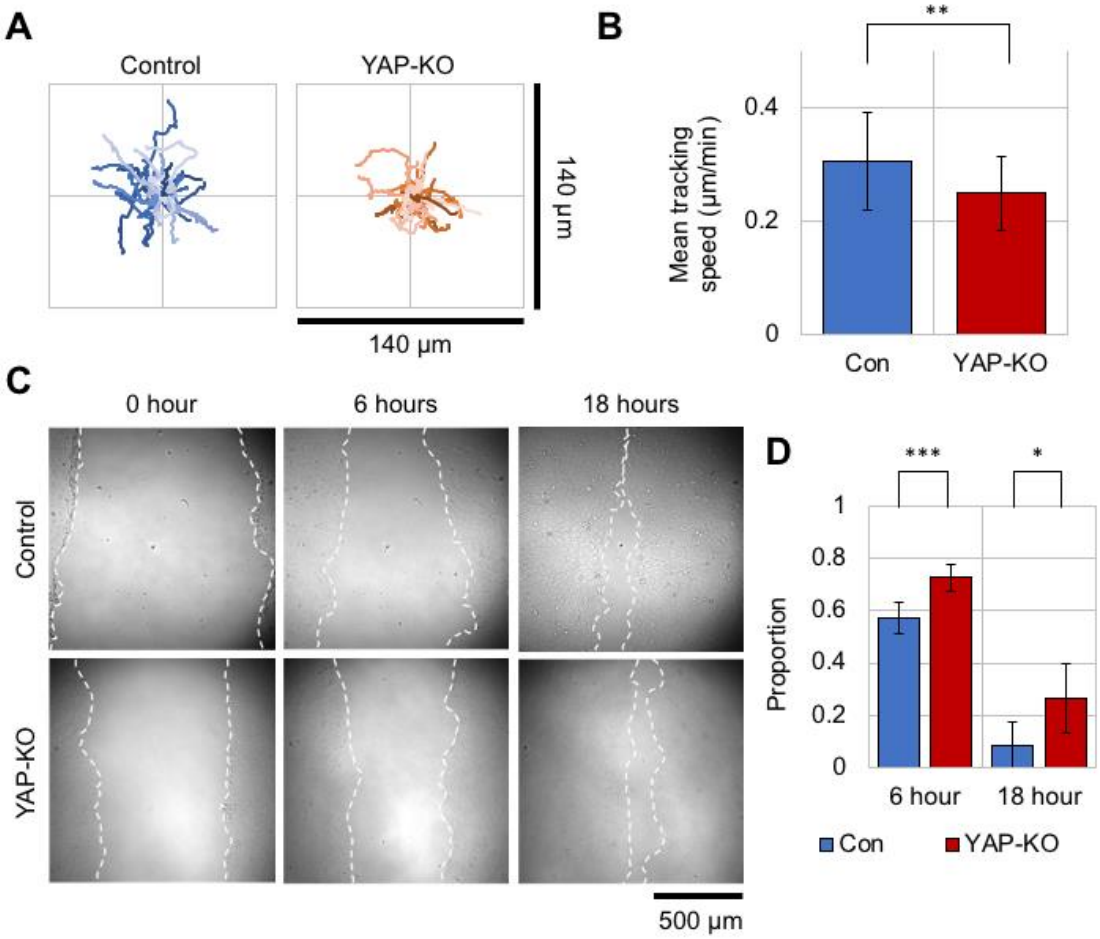

Fig 21. Track cell migration and wound healing of MDCK cells revealed a slower migration in YAP-KO cells

(A) Cell migrating routes in 3 hours, 5 minutes per image. N=30 for control cells, N=29 for YAP-KO cells.

(B) Mean speed calculated by ImageJ plugin Trackmate automatically. Error bar ± SD. **, p value <0.01, Student's t-test.

(C) Wound healing assay for MDCK control (upper) and YAP-KO (down) cells. Images were taken at 0, 6, 18 hours after scratch. N=5 areas for control group, N=9 areas for YAP-KO group.

(D) The ratio of the wound area at 6 hours or 18 hours to scratching area at 0 hour was quantified. Error bar ± SD. ***, p value <0.001 after 6 hours and *, p value <0.05 after 18 hours, Student's t-test.

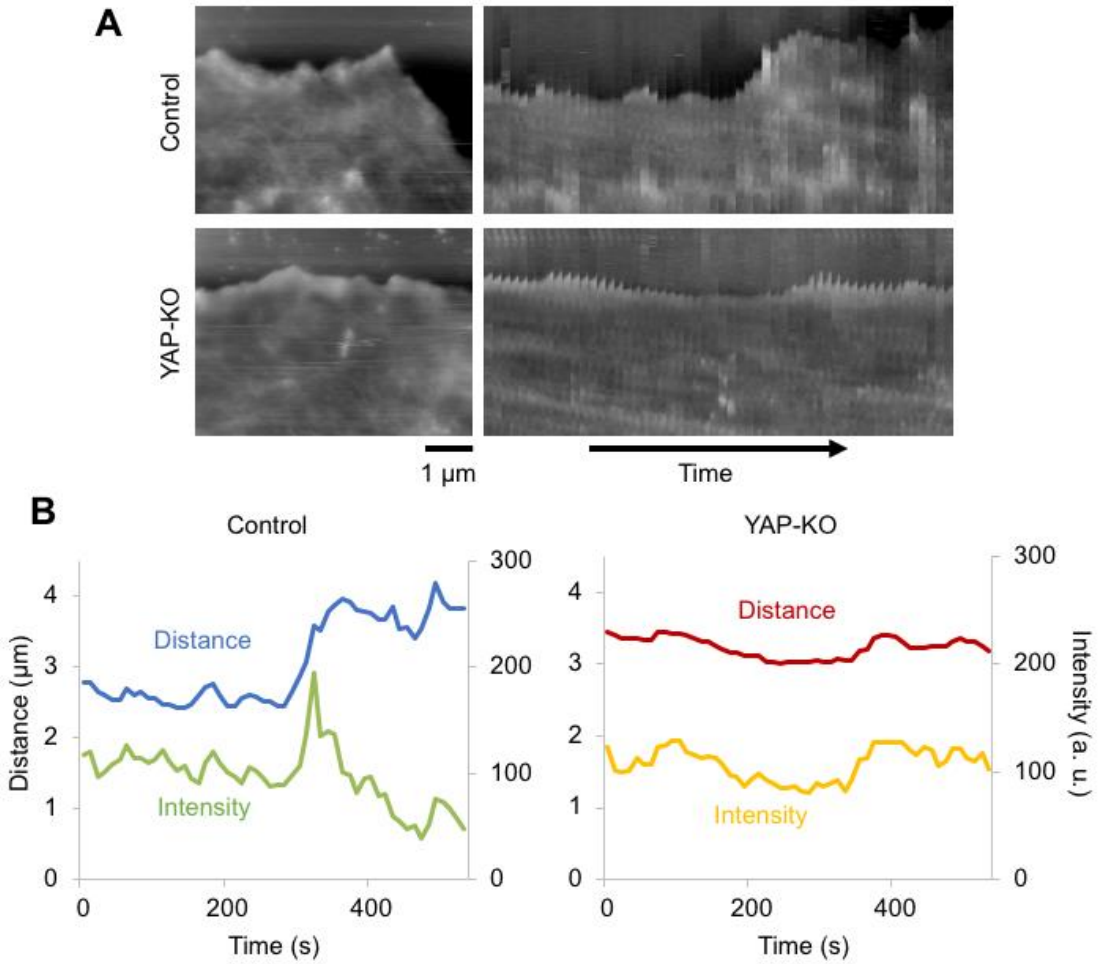

Fig 22. Cell edge movement of MDCK control and YAP-KO cells didn't show significant differences

(A) Representative cell edges (left) of control (upper) and YAP-KO (down) MDCK cells. The kymograph (right) showed a 10-pixel line was chosen in the HS-AFM movie and arranged in a chronological order. AFM images were taken 10 seconds per frame.

(B) The movement of the cell edge and the intensity of a position 0.24 μm from the edge were tracked and graphed.

be detected (**Fig. 22B**). These results indicated that slow migration of YAP-KO cells is not due to the reduced actin dynamics in lamellipodia.

3.3.2 RhoA activity in YAP-KO cells

3.3.2.1 RhoA is more active in YAP-KO cells

From previous researches, Rho GTPase family proteins are potential candidates in the downstream pathway of YAP to regulate the actin filaments (Qiao et al., 2017; Mason et al., 2019). Pull-down assay was performed to quantify active Rac1, Cdc42 and RhoA in RPE cells. Rac1-binding domain of protein kinase A (GST-pGBD) which binds to active Rac1, Cdc42-binding domain of N-WASP (GST-wGBD) which binds to active Cdc42, and RhoA-binding domain of rhotekin (GST-rGBD) which binds to active RhoA were prepared as fusion proteins with GST. By using these baits, the active Rac1, Cdc42 and RhoA in the control and the KO cells were quantified. The amounts of active Rac1 and Cdc42 were similar in the control and YAP-KO cells, whereas active RhoA level was higher in KO cells (**Fig. 23**), indicating that RhoA is highly activated in YAP-KO cells.

3.3.2.2 Activation of RhoA increases the cortex resistance

A relationship between RhoA and cortical actin was then examined. Constitutive active form of RhoA (Q63L) fused with EGFP was expressed in MDCK cells (control and KO cells), and the analysis of photo-damage/recovery as described in the previous section

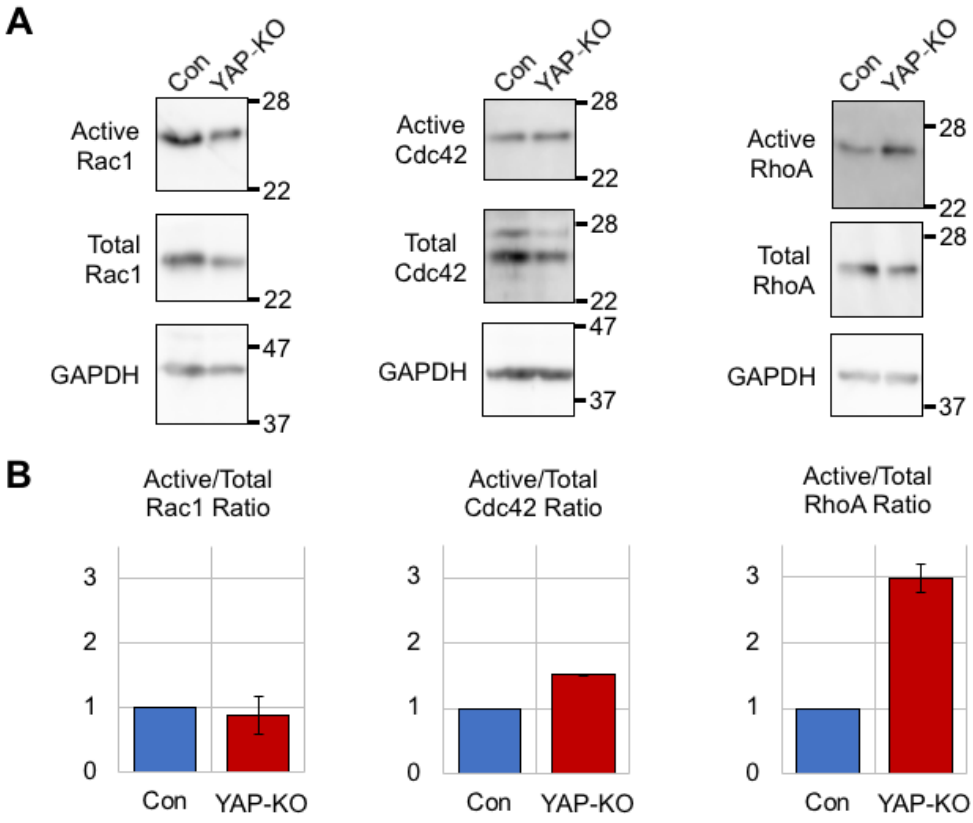

Fig 23. Measurement of active Rac1, Cdc42, RhoA in RPE control and YAP-KO cells by pull down assay

(A) Active and total Rac1/Cdc42/RhoA were detected by pull down assay. GAPDH was the loading control.

(B) Data quantification of the ratio of active and total Rac1/Cdc42/RhoA. Error bar ± SD. Two independent experiments.

was performed. Cells were given a laser-damage with a 3 μm-diameter circle for 5 seconds as previously described. The expression of EGFP-RhoA (Q63L) in control cells drastically reduced the entry of PI (**Fig. 24**). The detailed kinetic analysis revealed that both the effective radius and the closure rate decreased by expression of RhoA (Q63L) (**Fig. 25**). When RhoA (Q63L) was expressed in YAP-KO cells, the PI entry was also decreased, but the effect was very small compared to the control cells (**Fig. 26**). The effective radius was also slightly reduced. These results suggest that YAP-KO MDCK cells contain high level of active RhoA than the control cells.

The cortical actin dynamics of RhoA (Q63L)-expressing cells was also visualized and analyzed by HS-AFM. A striking difference was observed as actin bundles (**Fig. 27**); actin filaments were forming thicker bundles in RhoA (Q63L)-expressing cells, which is different from a random mesh observed in the control cells (**Fig. 27**). This observation well explains the result of the photo-damage assay described above (**Fig. 24-26**), but slightly different from the phenotype of YAP-KO cells, in which the density of random actin filaments was increased (**Fig. 12**).

3.3.2.3 Intracellular distribution of RhoGAP is affected by YAP

The activity of RhoA is generally regulated by a large number of RhoGEF and RhoGAP (Ridley, 2006). Previous research found that one of the RhoGAP ARHGAP18 is in the

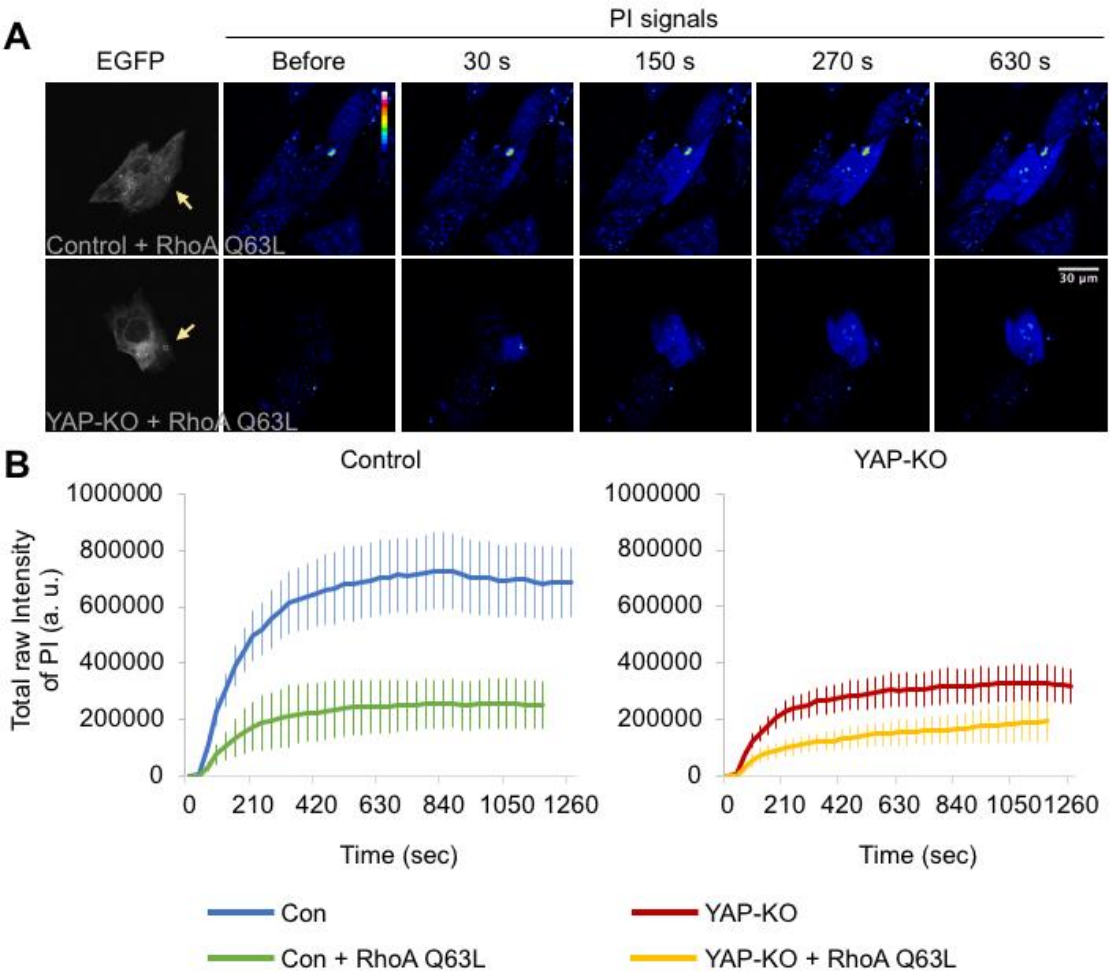

Fig 24. Photo-damage recovery of MDCK control and YAP-KO cells overexpressed RhoA constitutively active mutant Q63L

(A) Time-lapse images of the photo-damage performed on the MDCK control + RhoA Q63L (upper) and YAP-KO + RhoA Q63L (down) cells. The first image (left) shows the cell morphology with RhoA Q63L-EGFP signals. Laser was performed on the yellow circles with arrows. The PI intensity was shown by color bar with the time point before laser damage, 30 s, 150 s, 270 s, 630 s after laser damage.

(B) The intensity change of PI with time. The total analyzing time for overexpressed cells was 1170 s. Error bar ± 95% Confidence Intervals. N=22 cells for control + RhoA Q63L group, N=17 cells for YAP-KO + RhoA Q63L group.

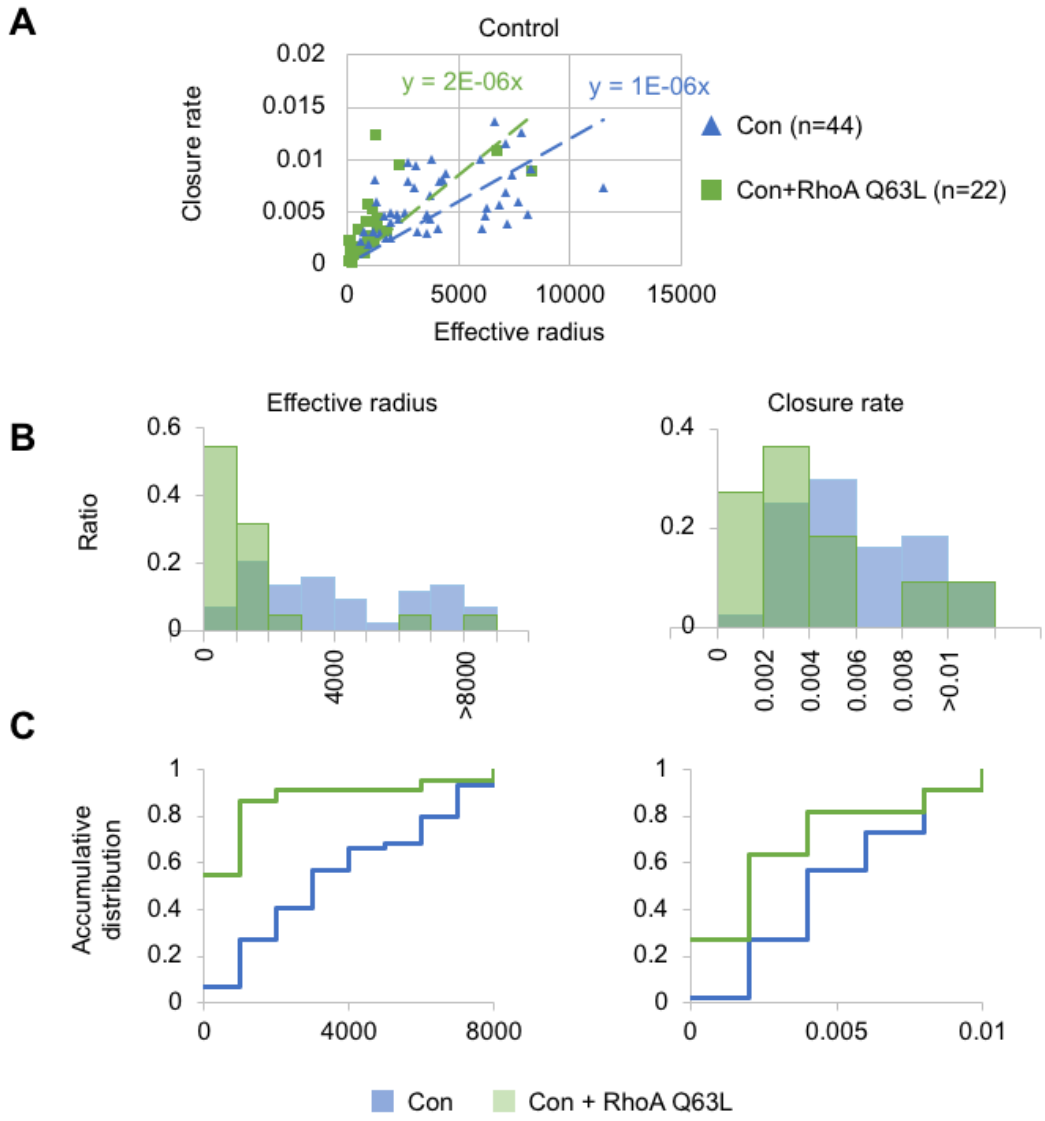

Fig 25. Analysis of MDCK control cells overexpressing RhoA constitutively active mutant Q63L PI fluorescence curves

(A) The PI fluorescence curve was fitted to a mathematical formula. Plot shows the closure rate and effective radius of laser-induced wounds. A liner approximation was fitted to explain the relation between the two factors in untreated control and control cells overexpressing RhoA Q63L.

(B) The distribution of the effective radius (left) and closure rate (right) of laser-induced wounds.

(C) Significance test of the distribution of effective radius and closure rate was taken by two-sample Kolmogorov-Smirnov test and the graph shows the cumulative distribution of effective radius (left) and closure rate (right). Significant decrease was seen in both effective radius (left) and closure rate (right).

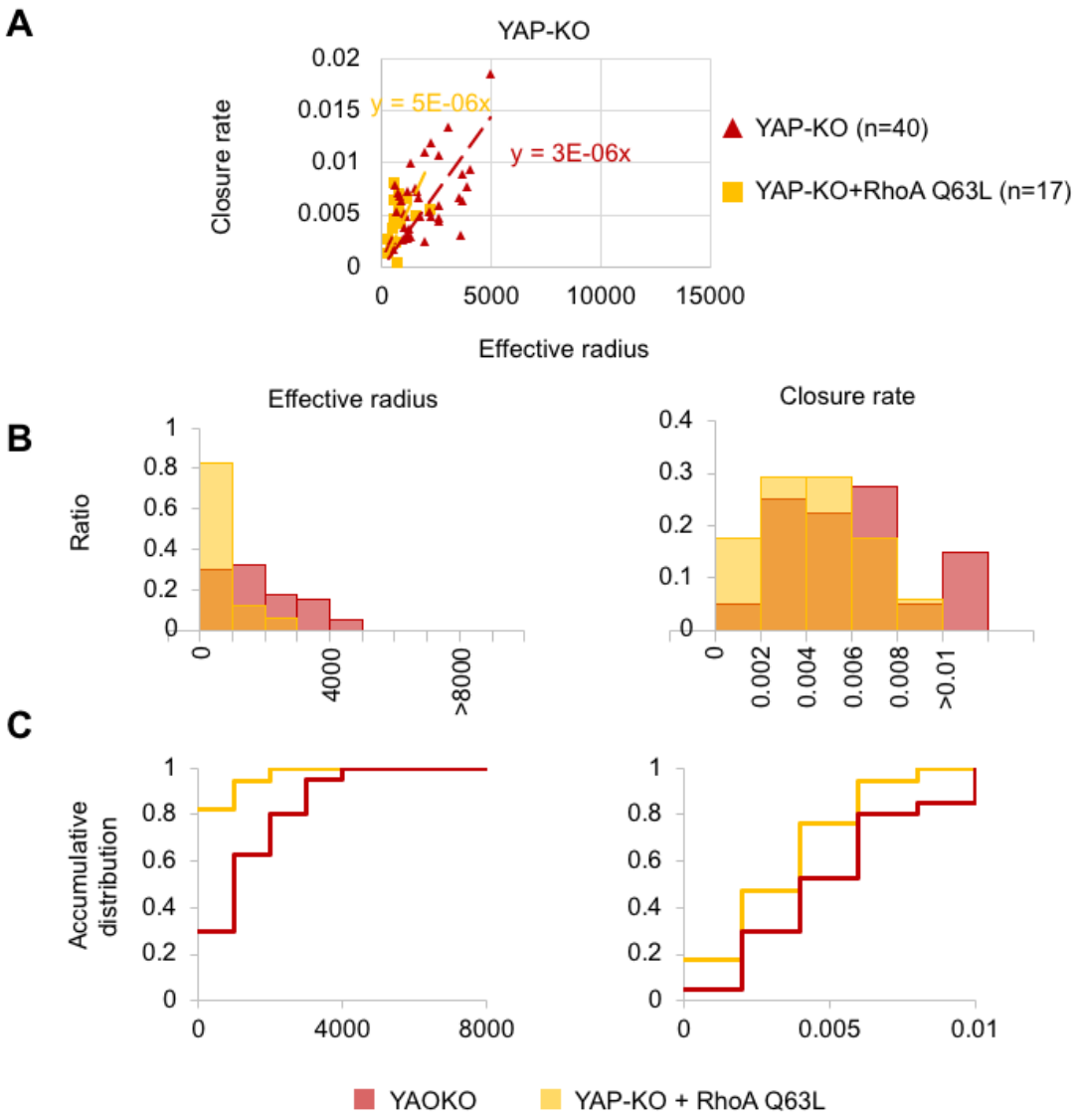

Fig 26. Analysis of MDCK YAP-KO cells overexpressing RhoA constitutively active mutant Q63L PI fluorescence curves

(A) The PI fluorescence curve was fitted to a mathematical formula. Plot shows the closure rate and effective radius of laser-induced wounds. A liner approximation was fitted to explain the relation between the two factors in untreated YAP-KO and YAP-KO cells overexpressing RhoA Q63L.

(B) The distribution of the effective radius (left) and closure rate (right) of laser-induced wounds.

(C) Significance test of the distribution of effective radius and closure rate was taken by two-sample Kolmogorov-Smirnov test and the graph shows the cumulative distribution of effective radius (left) and closure rate (right). A Significant decrease in effective radius (left) was detected.

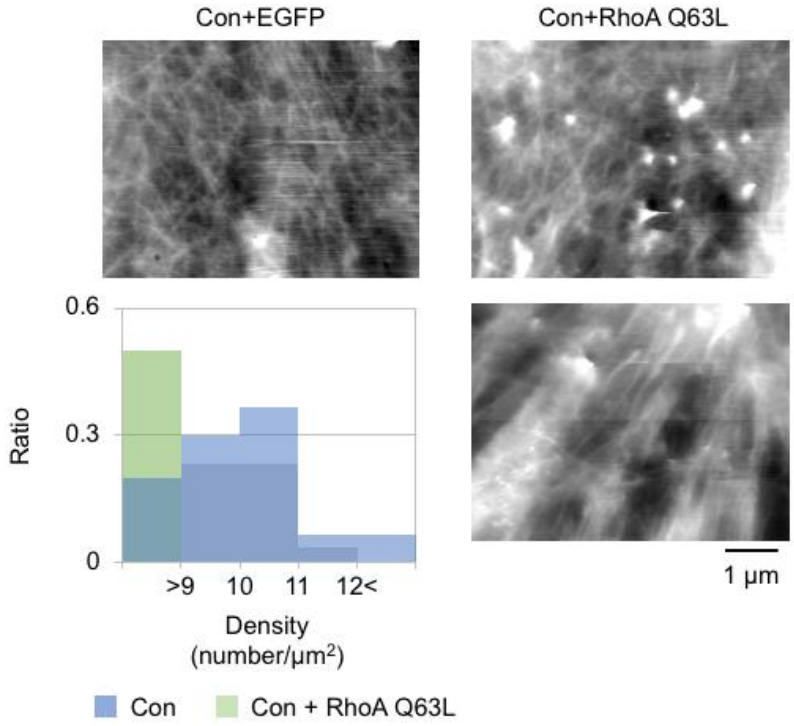

Fig 27. An increase of actin bundles in the control cells overexpressed RhoA (Q63L)-EGFP
Representative cortical actin meshwork of control overexpressed EGFP (left up) and control overexpressed RhoA Q63L (right up) MDCK cells visualized by HS-AFM. The scan area was 6×4.5 μm^2. The image below shows the actin bundles visualized after lowing the z-position in the same cell as the right up cell. Distribution of cortical actin density (left down). N=2 cells, 30 areas for control+EGFP group, N=2 cells, 30 areas for control+RhoA Q63L group. *, $p<0.05$

downstream of YAP (Porazinski et al., 2015). Another line of evidence demonstrated that RhoA is one of the substrate of ARHGAP18 (Maeda et al., 2011). Therefore, the effect of YAP depletion on the intracellular amount and distribution of ARHGAP18 was examined in MDCK cells.

The amount of ARHGAP18 was compared between the control and the KO cells by western blotting. As shown in **Fig. 28**, YAP-KO cells are expressing comparable amount of ARHGAP18 to the control cells. The intracellular distribution of ARHGAP18 in RPE cells was then examined by immunostaining. As reported previously, ARHGAP18 was mainly localized in the cytoplasm of the control cells (**Fig. 29**). A migrating cell showed a weak accumulation of ARHGAP18 at the leading edge (**Fig. 29A**), which is consistent with the previous research (Maeda et al., 2011). In contrast, YAP-KO cells showed a stronger accumulation of ARHGAP18 at the cell edge (**Fig. 29A**). The intensity profile of ARHGAP18 across the cell axis revealed clear peaks at the cell edges in KO cells but not in the control cells (**Fig. 29B**). In contrast, actin signal did not show significant differences at the cell edges in both cell types (**Fig. 29B**). When YAP was reintroduced into YAP-KO cells by transfection of pmCherry-YAP, the accumulation of ARHGAP18 at the cell edges decreased to a similar level to that of the control cells (**Fig. 30**),

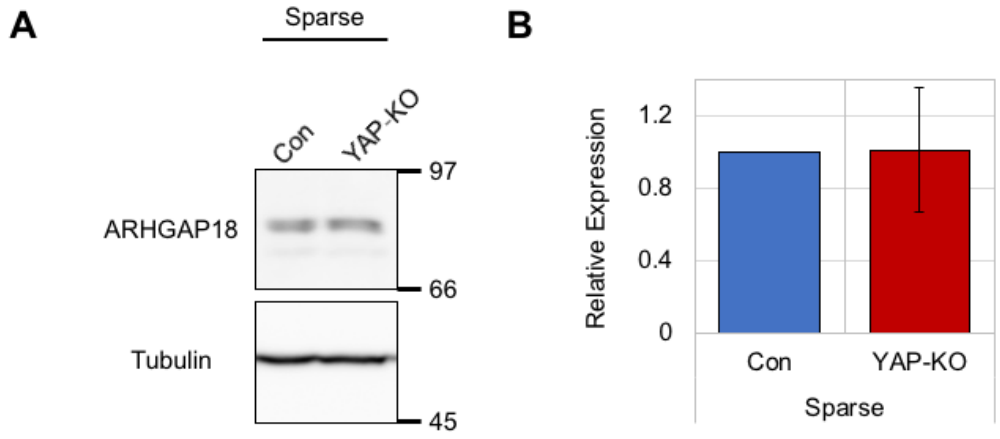

Fig 28. Expression check of ARHGAP18 at a sparse density by western blot showed the same level of ARHGAP18 expression in control and YAP-KO cells

(A) Western blot shows the expression of ARHGAP18 in control and YAP-KO RPE cells at a sparse density. Tubulin was the loading control.

(B) Data quantification of western blot. Error bar ± SD. Three independent experiments.

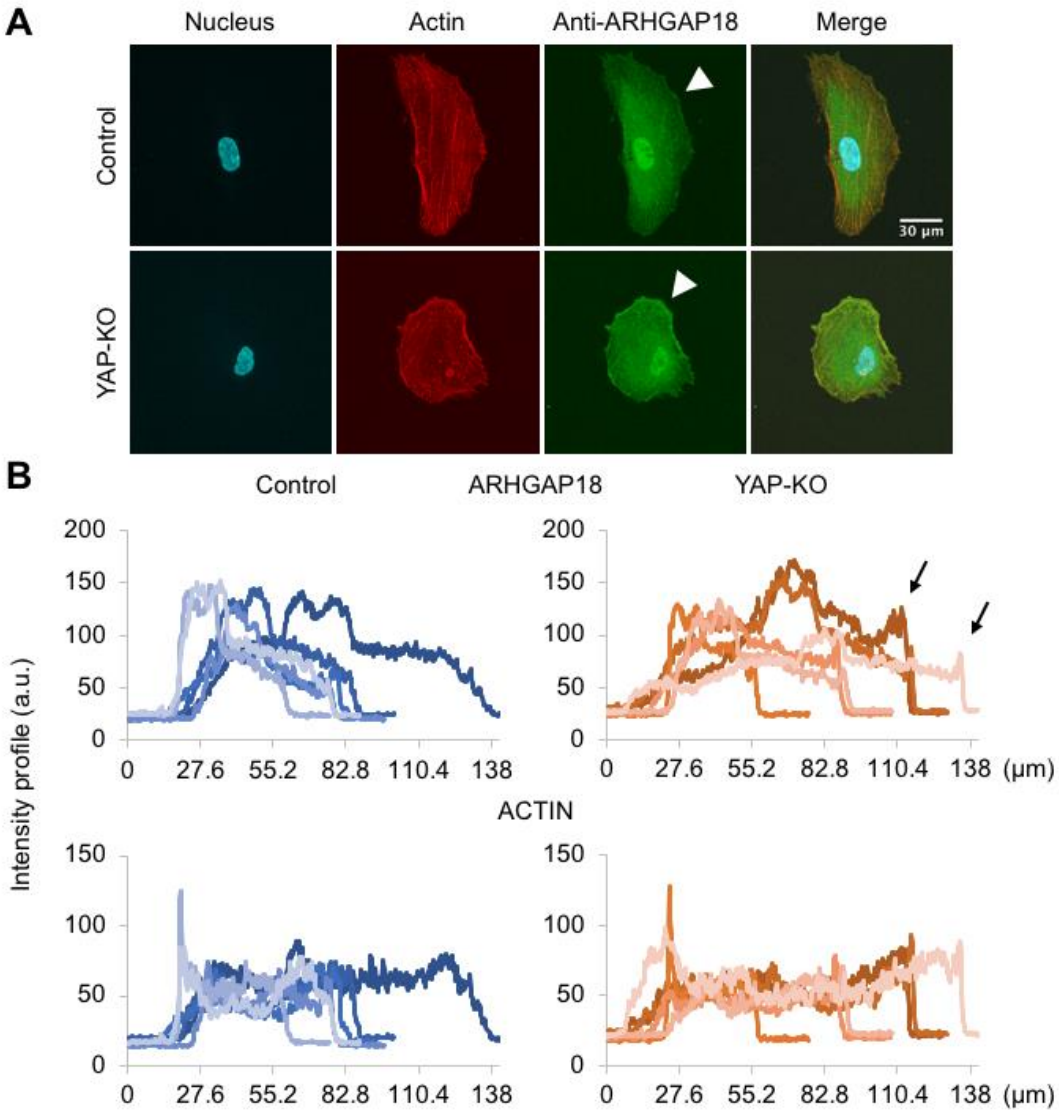

Fig 29. Translocalization of ARHGAP18 in YAP-KO cells

(A) Representative Z-stack images of control (upper) and YAP-KO (down) RPE cells. Stress fibers were stained with Rhodamine-phalloidin, and nuclei were stained with Hoechst33342. White arrows shows the normal localization of ARHGAP18 in control cells (upper) and the over-accumulation of ARHGAP18 in YAP-KO cells (down).

(B) The cell intensity profile was traced within a line of 50 pixels passing through the cell. The intensity profile of ARHGAP18 (upper) in YAP-KO cells showed a clear peak (arrows) at the cell edge but not in control cell, while actin bundles (down) didn't show significant changes between control and YAP-KO cells.

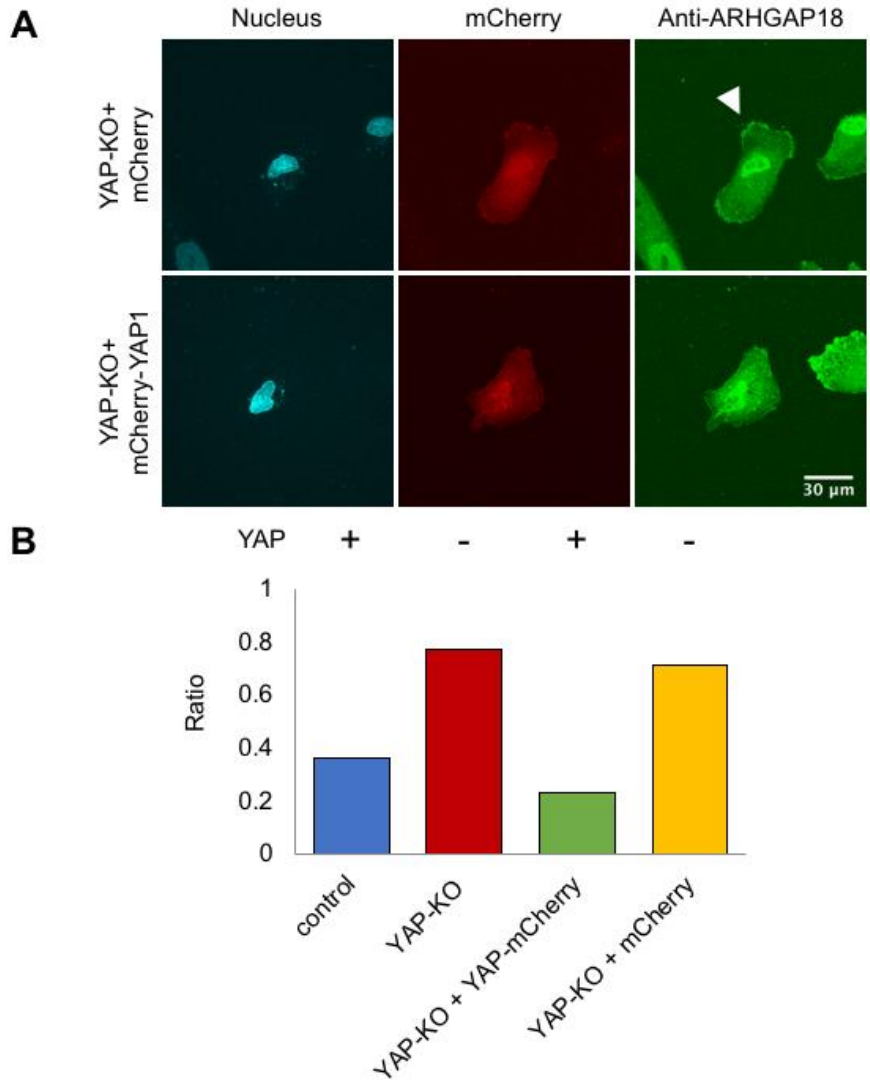

Fig 30. Re-introduction of YAP in YAP-KO RPE cells rescued the over-accumulation of ARHGAP18 at cell edges

(A) Representative Z-stack images of YAP-KO cells expressing mCherry (upper) and YAP-KO cells expressing mCherry-YAP1 (down). Nuclei were stained with Hoechst33342. White arrows shows the over-accumulation of ARHGAP18 in YAP-KO cells expressing mCherry (upper).

(B) Ratio of the over-accumulated cells were calculated. N=22 for untreated control cells, N=18 for untreated YAP-KO cells, N=15 for YAP-KO cells expressing mCherry-YAP1, N=14 for YAP-KO cells expressing mCherry.

demonstrating that the reduction of YAP level affected the intracellular distribution of ARHGAP18.

To make sure the over-accumulation of ARHGAP18 in YAP-KO cells was not due to the shrinkage of the cells, the cell areas were analyzed. A statistical analysis showed no difference in the area nor the shape (aspect ratio) between the control and the KO cells (**Fig. 31A, 31B**). Also, the change of the cell area over time was tracked. Both control and KO cell areas were decreasing as the cell density increased. However, there were no significant differences between the control and YAP-KO cells (**Fig. 31C**), confirming that the accumulation of ARHGAP18 at the cell edge is not due to a different morphology of the cells.

3.3.2.4 ARHGAP18 regulates RhoA activity

The effect of ARHGAP18 on RhoA activity was examined by pull-down assay. Flag-tagged ARHGAP18 was over-expressed in RPE cells, and the cell lysate was subjected to the pull-down assay using GST-fusion proteins (GST-rGBD or GST-wGBD or GST-pGBD) as described in the previous section. The amounts of active Rac1 and Cdc42 were not affected by over-expression of ARHGAP18 (**Fig. 32**), whereas active RhoA decreased in both control and YAP-KO cells (**Fig. 32**), demonstrating that ARHGAP18 works as a RhoGAP of RhoA but not Rac1 or Cdc42 in RPE cells.

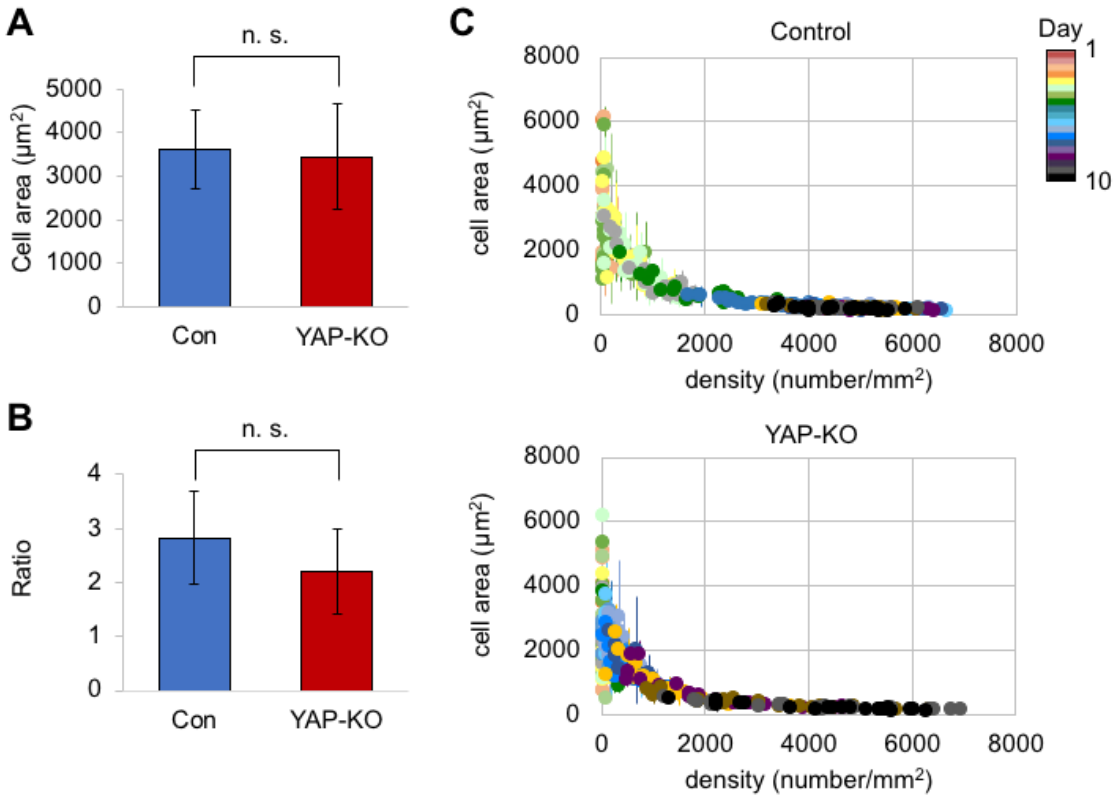

Fig 31. Cell areas analysis of control and YAP-KO cells didn't show significant differences

(A) Cell area analysis of RPE control and YAP-KO cells. Error bar ± SD. N=7 for control cells, N=6 for YAP-KO cells. Student's t-test.

(B) The ratio of cell length to width was analyzed for RPE cells. Error bar ± SD. N=7 for control cells, N=6 for YAP-KO cells. Student's t-test.

(C) Graphs shows the cell areas attached to the bottom decreased with the increase of cell density in MDCK cells. Color bar means the days after passing the cells on the dishes with grids. The same grids were recorded and analyzed over time. Error bar ± SD, N=20 grids for control cells, and N=20 grids for YAP-KO cells were measured.

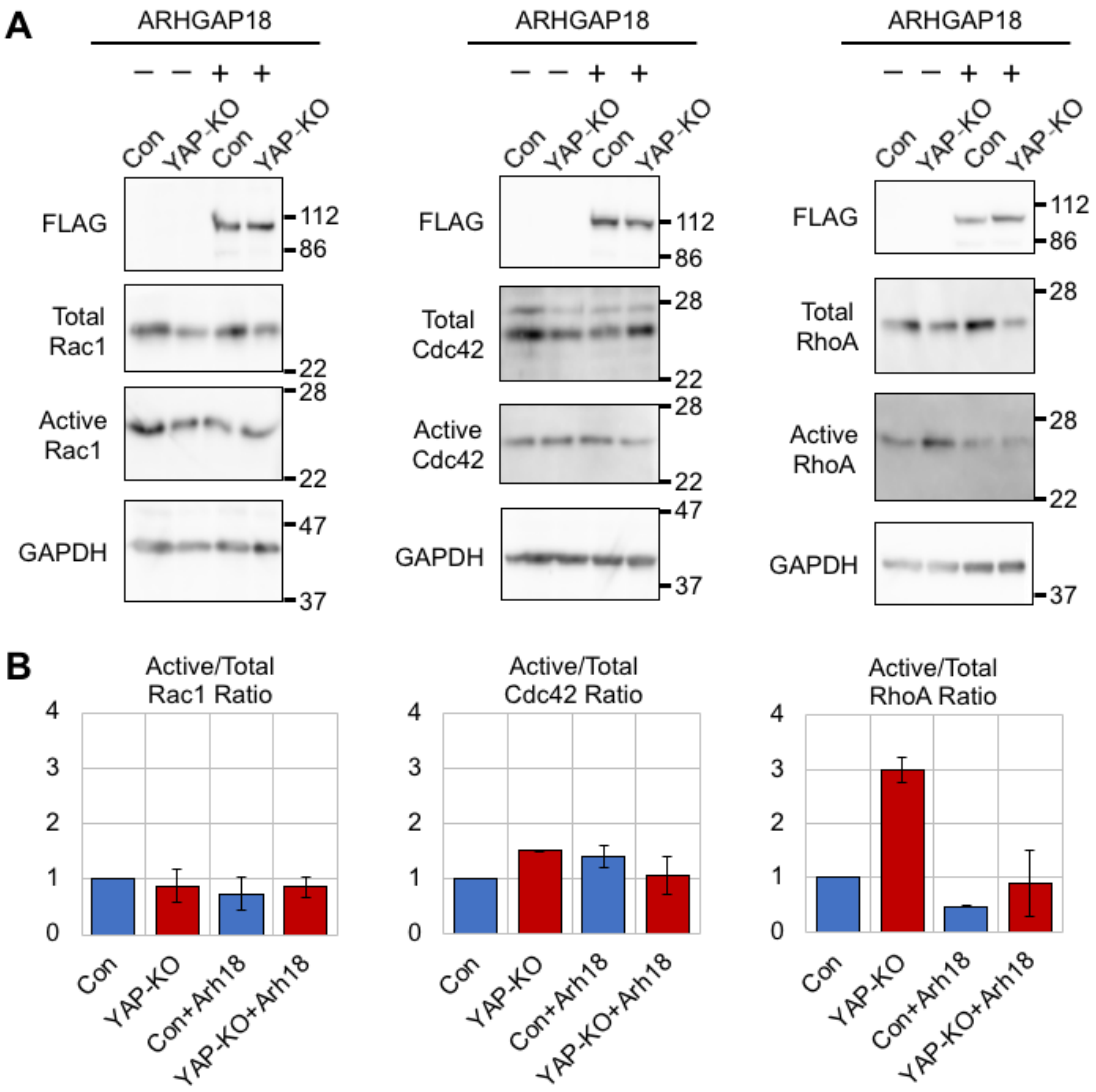

Fig 32. Measurement of Rac1, Cdc42, RhoA activity by pull down assay revealed RhoA activity is regulated by ARHGAP18

(A) Active and Total Rac1/Cdc42/RhoA were detected by pull down assay. RPE control and YAP-KO cells were untreated or overexpressed with FLAG-ARHGAP18. GAPDH was the loading control.

(B) Data quantification of the ratio of active and total Rac1/Cdc42/RhoA. Error bar ± SD. Two independent experiments.

3.3.2.5 Proteins affecting the intracellular localization of ARHGAP18

The observation that ARHGAP18 accumulated in lamellipodia of YAP-KO cells imply that an unidentified membrane-bound protein that is regulated by YAP associates with ARHGAP18 and anchors it to the cell surface. A transmembrane protein, E-Cadherin, may be one of the potential candidates (Nagafuchi and Takeichi, 1989). The protein level of E-cadherin increased in YAP-KD MDCK cells compared to the control cells, suggesting that E-cadherin is a target of YAP (Park et al., 2019). In addition, BioID analysis identified ARHGAP18 (out of 612 proteins) near E-cadherin's cytoplasmic tail (Guo et al., 2016). Therefore, the relationship between the intracellular E-cadherin level and the intracellular distribution of ARHGAP18 was examined in RPE cells.

The immunostaining of ARHGAP18 in YAP-KO RPE cells demonstrated that the accumulation of ARHGAP18 at lamellipodia was reduced by the overexpression of E-cadherin (**Fig. 33**). In contrast, the localization of ARHGAP18 was not affected by E-cadherin in control cells. These data suggested that E-cadherin might play a role in controlling the localization of ARHGAP18 under the YAP-dependent pathway.

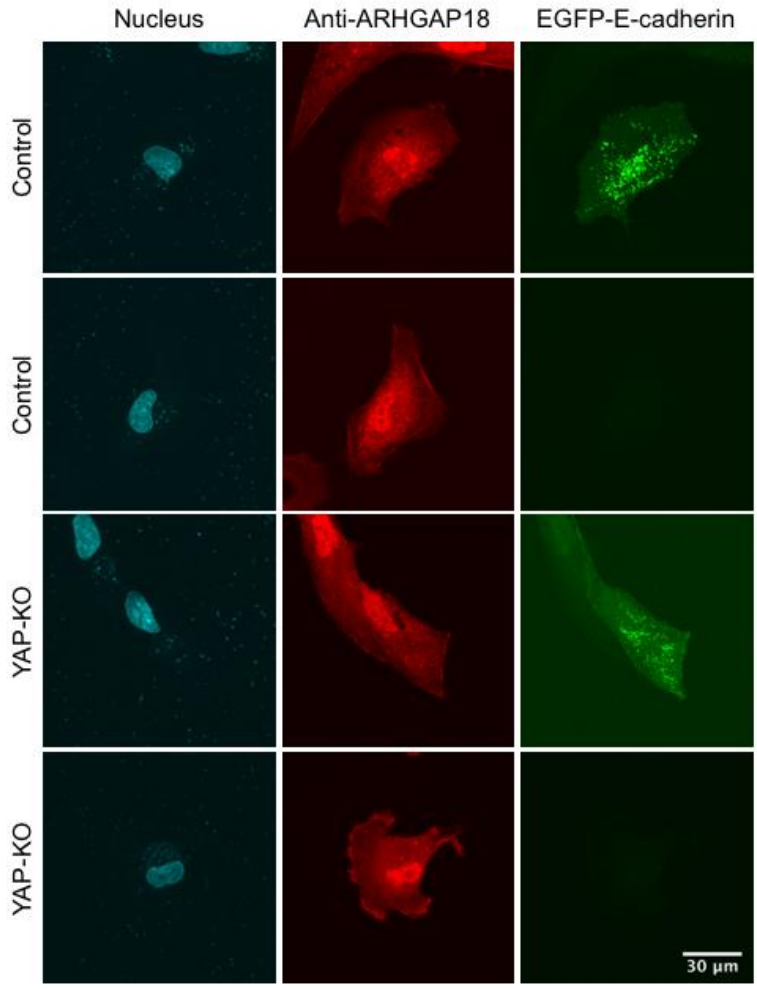

Fig 33. ARHGAP18 localization of YAP-KO RPE cells with overexpression of E-cadherin showed a decrease in the accumulation at cell edges.
Representative Z-stack images shows the ARHGAP18 localization in control and YAP-KO RPE cells with or without overexpressed E-cadherin. Nuclei were stained with Hoechst33342.

3.4 Discussion

In this chapter, the mechanism of how cortical actin is maintained and regulated by a transcriptional co-regulator YAP was investigated. YAP negatively regulated the stiffness of the cell cortex; HS-AFM experiments showed an increased density of cortical actin filaments in YAP-KO cells, and the mechanical characterization also demonstrated higher Young's modulus in YAP-KO cells. Plasma membrane damage induced by laser implied that YAP-KO cells might have a stronger resistance to membrane damage. This negative regulation by YAP is controlled by the activity of RhoA at the cell cortex. The localization of a RhoGAP, ARHGAP18 was regulated by YAP and controlled the local activity of RhoA at cell cortex probably through binding to a membrane binding protein E-cadherin.

3.4.1 A negative regulation in cortical actin by YAP

It is very intriguing that although the cortical stiffness of YAP-KO cells was stiffer than the control cells both in MDCK cell and the gastric cancer cell line MKN28, the phenotype of stress fibers that stained with phalloidin were very different between these two cell lines (Qiao et al., 2017). This may suggest a different mechanism to regulate actin dynamics in normal cells from cancer cells. The data by HS-AFM showed that the cortical actin filaments in YAP-KO cells were denser than control cells. In addition, actin

filaments were polymerized more frequently in YAP-KO cells than control cells. YAP-KO cells was proved to phosphorylate cofilin (Ser3), which may reduce the depolymerization of actin filament in YAP-KO cells (Qiao et al., 2017). Although the depolymerization of actin filament cannot be observed by HS-AFM, the data by HS-AFM suggested that besides the regulation of disassembly, YAP could also regulate the assembly of actin filaments.

Photo-damage experiments showed that YAP-KO MDCK cells were difficult to open a bigger wound than control MDCK cells. Several mechanisms were proposed to explain the process of membrane wound repair. For small wounds (<100 nm), caveolar endocytosis (Corrotte et al., 2013) or ESCRT-mediated budding (Jimenez et al., 2014) are thought to repair the wounds. For big wounds, a 'vertex fusion' model was proposed (Fomby and Cherlin, 2011). The detailed analysis of the recovery curve demonstrated the change in the effective radius but not in the lesion closure rate (**Fig. 17**). This indicates that the cortex is more resistant to the external damage, due to the denser filament network, and the recovery rate is not affected in KO cells. The recovery of the wound involves a number of proteins and signaling cascades including Ca^{2+} signaling. My result shown here suggest that YAP controls the stiffness of the cortex itself, but not the recovery machinery and signaling.

3.4.2 RhoA in the downstream of YAP to regulate cortical actin

When constitutively active RhoA mutant Q63L was overexpressed in control MDCK cells, not only the effective radius of photo-damage lesion decreased, the closure rate of the lesion also decreased, which was different from the phenomenon observed in YAP-KO cells. The cortical actin dynamics visualized by HS-AFM showed an increase in actin bundles instead of the meshwork observed in the control cells overexpressed with EGFP-RhoA Q63L. This may increase the contractility of actomyosin to strengthen its resistance to plasma membrane damage. While in YAP-KO cells, the denser cortical actin meshwork is the reason for stronger resistance to the damage. The cell stiffness was proved to be related to the cellular resistance to plasma membrane injury (Stroetz et al., 2001). Besides cortical actin, the cortical actin-plasma membrane integrity should also be considered. RhoA was found to increase cortical rigidity during mitosis (Maddox and Burridge, 2003) and activate the ERM proteins, which connect the plasma membrane and actin filaments (Matsui et al., 1999). The overexpression of RhoA may increase the stiffness of the cortex by strengthening the connection between cortical actin and the plasma membrane.

3.4.3 ARHGAP18 in the downstream of YAP

So far, several RhoGAPs and RhoGEFs were found as in the downstream of YAP. For example, ARHGAP18 (Porazinski et al., 2015), ARHGAP28 (Mason et al., 2019), ARHGAP29 (Qiao et al., 2017), and TRIO (a RhoGEF of Rac1) were under the control of YAP (Shah et al., 2019). However, the intracellular protein level of ARHGAP18 was not changed in YAP-KO RPE cells. Previous study showed that the protein expression of ARHGAP18 was decreased in the spheroid of YAP-KD RPE cells compared to WT cells (Porazinski et al., 2015). Since YAP localization and function are closely related to the cell density, this difference may suggest that in sparse and dense condition YAP has the different regulation on ARHGAP18.

In contrast to the protein expression of ARHGAP18 in control and YAP-KO cells in sparse density, more ARHGAP18 proteins were accumulated in lamellipodia in YAP-KO cells than control cells. I demonstrated that YAP regulates the expression of a membrane-bound protein (such as E-cadherin) which anchors ARHGAP18 to the plasma membrane throughout the cell cortex. When YAP is depleted, the expression of E-cadherin is decreased, and ARHGAP18 no longer localizes to the cortex and accumulates at the lamellipodia.

3.4.4 Perspectives

There are still several questions to be answered to elucidate the whole mechanism of cortical actin regulation. i) what is the downstream factor of RhoA. Although the evidence was showed that YAP regulates the cortical actin dynamics via active RhoA, there are many effectors for RhoA and most of them can regulate the turnover of actin filaments, such as formins (Kühn and Geyer, 2014), cofilin (Lin et al., 2003). It is necessary to identify the down regulator of RhoA that are working specifically at cell cortex. ii), How the localizations of E-cadherin and ARHGAP18 are changed depending on the cell density. Since YAP is involved in the 3D construction of tissues, it is highly intriguing to investigate how YAP activity and downstream factors that I identified in this study (E-cadherin, ARHGAP18 and active RhoA) are affected when the cell density increases and when cells are cultured in 3D. This will elucidate how YAP controls 3D tissue organization through cortical actin structures.

Chapter 4

Summary

In this study, I established a method to analyze the dynamics of individual actin filaments in a living cell cortex by utilizing HS-AFM, and elucidated the molecular mechanism of how the cortical actin is regulated by YAP-regulated genes. The achievements that I made in the study can be summarized as follows.

i) The dynamics of a single actin filament in the cell cortex was visualized in a living cell without labeling, fixing and staining. This has a great advantage over fluorescence-based observation techniques previously utilized, which require expression or introduction of exogenous labeled or tagged proteins in the target cell.

ii) Not only the structure but also kinetic parameters (the frequency of newly assembled filaments and the elongation rate) of individual actin filaments could be obtained by image analysis.

iii) YAP downregulates the density and the stiffness of cortical actin by controlling the expression of E-cadherin, intracellular localization of ARHGAP18 and RhoA activity. This finding links the transcriptional control by YAP and structural alteration of cortical actin.

The HS-AFM-based approach that I established here is useful for analyzing the function of various actin-regulating proteins. It is unique and can be applied for other cellular events related to cortical actin, such as mechanosensing, cell migration, mitosis. By combining with other functional imaging techniques, it will further contribute to functional analysis of various protein functions in future studies.

Bibliography

Abreu-Blanco, M.T., J.M. Verboon, and S.M. Parkhurst. (2011). Single cell wound repair: Dealing with life's little traumas. *Bioarchitecture*. 1:114–121.

Ahuja, R., R. Pinyol, N. Reichenbach, L. Custer, M.M. Kessels, and B. Qualmann. (2007). Cordon-bleu is an actin nucleation factor and controls neuronal morphology. 131:337–350.

Aihara, E., N.M. Medina-Candelaria, H. Hanyu, A.L. Matthis, K.A. Engevik, C.B. Gurniak, W. Witke, J.R. Turner, T. Zhang, and M.H. Montrose. (2018). Cell injury triggers actin polymerization to initiate epithelial restitution. *J. Cell Sci.* 131.

Amann, K.J., and T.D. Pollard. (2001). The Arp2/3 complex nucleates actin filament branches from the sides of pre-existing filaments. *Nat. Cell Biol.* 3:306–310.

Aragona, M., T. Panciera, A. Manfrin, S. Giulitti, F. Michielin, N. Elvassore, S. Dupont, and S. Piccolo. (2013). A mechanical checkpoint controls multicellular growth through YAP/TAZ regulation by actin-processing factors. *Cell*. 154:1047–1059.

Barzik, M., T.I. Kotova, H.N. Higgs, L. Hazelwood, D. Hanein, F.B. Gertler, and D.A. Schafer. (2005). Ena/VASP proteins enhance actin polymerization in the presence of barbed end capping proteins. *J. Biol. Chem.* 280:28653–28662.

Bear, J.E., T.M. Svitkina, M. Krause, D.A. Schafer, J.J. Loureiro, G.A. Strasser, I. V. Maly, O.Y. Chaga, J.A. Cooper, G.G. Borisy, and F.B. Gertler. (2002). Antagonism between Ena/VASP proteins and actin filament capping regulates fibroblast motility. *Cell*. 109:509–521.

Blanchoin, L., R. Boujemaa-Paterski, C. Sykes, and J. Plastino. (2014). Actin dynamics, architecture, and mechanics in cell motility. 94. 235–263.

Boudaoud, A., A. Burian, D. Borowska-Wykręt, M. Uyttewaal, R. Wrzalik, D. Kwiatkowska, and O. Hamant. (2014). FibrilTool, an ImageJ plug-in to quantify fibrillar structures in raw microscopy images. *Nat. Protoc.* 9:457–463.

Breitsprecher, D., A.K. Kiesewetter, J. Linkner, M. Vinzenz, T.E.B. Stradal, J.V. Small, U. Curth, R.B. Dickinson, and J. Faix. (2011). Molecular mechanism of Ena/VASP-mediated actin-filament elongation. *EMBO J.* 30:456–467.

Bubb, M.R., I. Spector, B.B. Beyer, and K.M. Fosen. (2000). Effect of Jasplakinolide on the kinetics of actin polymerization. *Biochemistry*. 275:5163–5170.

Cao, L.G., and Y.L. Wang. (1990). Mechanism of the formation of contractile ring in dividing cultured animal cells. II. Cortical movement of microinjected actin filaments. *J. Cell Biol.* 111:1905–1911.

Carlier, M.F., C. Jean, K.J. Rieger, M. Lenfant, and D. Pantaloni. (1993). Modulation of the interaction between G-actin and thymosin β4 by the ATP/ADP ratio: Possible implication in the regulation of actin dynamics. *Proc. Natl. Acad. Sci. U. S. A.* 90:5034–5038.

Carlier, M.F., V. Laurent, J. Santolini, R. Melki, D. Didry, G.X. Xia, Y. Hong, N.H. Chua, and D. Pantaloni. (1997). Actin depolymerizing factor (ADF/cofilin) enhances the rate of filament turnover: Implication in actin-based motility. *J. Cell Biol.* 136:1307–1322.

Cartagena-Rivera, A.X., J.S. Logue, C.M. Waterman, and R.S. Chadwick. (2016). Actomyosin Cortical Mechanical Properties in Nonadherent Cells Determined by Atomic Force Microscopy. *Biophys. J.* 110:2528–2539.

Chen, Q., N. Courtemanche, and T.D. Pollard. (2015). Aip1 promotes actin filament severing by cofilin and regulates constriction of the cytokinetic contractile ring. *J. Biol. Chem.* 290:2289–2300.

Chugh, P., A.G. Clark, M.B. Smith, D.A.D. Cassani, K. Dierkes, A. Ragab, P.P. Roux, G. Charras, G. Salbreux, and E.K. Paluch. (2017). Actin cortex architecture regulates cell surface tension. *Nat. Cell Biol.* 19:689–697.

Chugh, P., and E.K. Paluch. (2018). The actin cortex at a glance. *J. Cell Sci.* 131:1–9.

Clark, A.G., K. Dierkes, and E.K. Paluch. (2013). Monitoring actin cortex thickness in live cells. *Biophys. J.* 105:570–580.

Corrotte, M., P.E. Almeida, C. Tam, T. Castro-Gomes, M.C. Fernandes, B.A. Millis, M. Cortez, H. Miller, W. Song, T.K. Maugel, and N.W. Andrews. (2013). Caveolae internalization repairs wounded cells and muscle fibers. *Elife*. 2013:1–30.

Cramer, L.P., M. Siebert, and T.J. Mitchison. (1997). Identification of novel graded polarity actin filament bundles in locomoting heart fibroblasts: Implications for the generation of motile force. *J. Cell Biol.* 136:1287–1305.

Das, A., R.S. Fischer, D. Pan, and C.M. Waterman. (2016). YAP nuclear localization in the absence of cell-cell contact is mediated by a filamentous actin-dependent, Myosin IIand Phospho-YAP-independent pathway during extracellular matrix mechanosensing. *J. Biol. Chem.* 291:6096–6110.

Dupont, S., L. Morsut, M. Aragona, E. Enzo, S. Giulitti, M. Cordenonsi, F. Zanconato, J. Le Digabel, M. Forcato, S. Bicciato, N. Elvassore, and S. Piccolo. (2011). Role of YAP/TAZ in mechanotransduction. *Nature*. 474:179–184.

Eghiaian, F., A. Rigato, and S. Scheuring. (2015). Structural, mechanical, and dynamical variability of the actin cortex in living cells. *Biophys. J.* 108:1330–1340.

Evans, E., and A. Yeung. (1989). Apparent viscosity and cortical tension of blood granulocytes determined by micropipet aspiration. *Biophys. J.* 56:151–160.

Fischer-Friedrich, E., A.A. Hyman, F. Jülicher, D.J. Müller, and J. Helenius. (2014). Quantification of surface tension and internal pressure generated by single mitotic cells. *Sci. Rep.* 4:4–11.

Fomby, P., and A.J. Cherlin. (2011). Damage Control: Cellular Mechanisms of Plasma Membrane Repair. 72:181–204.

Fritzsche, M., C. Erlenkämper, E. Moeendarbary, G. Charras, and K. Kruse. (2016a). Actin kinetics shapes cortical network structure and mechanics. *Sci. Adv.* 2.

Fritzsche, M., C. Erlenkamper, E. Moeendarbary, G.T. Charras, and K. Kruse. (2016b). Actin kinetics shapes cortical network structure and mechanics. *CELL Biol.* 2.

Fritzsche, M., A. Lewalle, T. Duke, K. Kruse, and G. Charras. (2013). Analysis of turnover dynamics of the submembranous actin cortex. *Mol. Biol. Cell*. 24:757–67.

Fujiwara, I., S. Takahashi, H. Tadakuma, T. Funatsu, and S. Ishiwata. (2002). Microscopic analysis of polymerization dynamics with individual actin filaments. *Nat. Cell Biol.* 4:666–673.

Geraldo, S., and P.R. Gordon-Weeks. (2009). Cytoskeletal dynamics in growth-cone steering. *J. Cell Sci.* 122:3595–3604.

Goeckeler, Z.M., P.C. Bridgman, and R.B. Wysolmerski. (2008). Nonmuscle myosin II is responsible for maintaining endothelial cell basal tone and stress fiber integrity. *Am. J. Physiol. - Cell Physiol.* 295:994–1006.

Guo, Z., L.J. Neilson, H. Zhong, P.S. Murray, and M.V. Rao. (2016). E-cadherin interactome complexity and robustness resolved by quantitative proteomics. 7:1–13.

Gupton, S.L., and F.B. Gertler. (2007). Filopodia: the fingers that do the walking. *Sci. STKE*. 2007.

Hotulainen, P., and P. Lappalainen. (2006). Stress fibers are generated by two distinct actin assembly mechanisms in motile cells. *J. Cell Biol.* 173:383–394.

Jansen, S., A. Collins, C. Yang, G. Rebowski, T. Svitkina, and R. Dominguez. (2011). Mechanism of actin filament bundling by fascin. *J. Biol. Chem.* 286:30087–30096.

Jimenez, A.J., P. Maiuri, J. Lafaurie-Janvore, S. Divoux, M. Piel, and F. Perez. (2014). ESCRT machinery is required for plasma membrane repair. *Science (80-.).* 343.

Kage, F., M. Winterhoff, V. Dimchev, J. Mueller, T. Thalheim, A. Freise, S. Brühmann, J. Kollasser, J. Block, G. Dimchev, M. Geyer, H.J. Schnittler, C. Brakebusch, T.E.B. Stradal, M.F. Carlier, M. Sixt, J. Käs, J. Faix, and K. Rottner. (2017). FMNL formins boost lamellipodial force generation. *Nat. Commun.* 8.

Kanai, F., P.A. Marignani, D. Sarbassova, R. Yagi, R.A. Hall, M. Donowitz, A. Hisaminato, T. Fujiwara, Y. Ito, L.C. Cantley, and M.B. Yaffe. (2000). TAZ: A novel transcriptional co-activator regulated by interactions with 14-3-3 and PDZ domain proteins. *EMBO J.* 19:6778–6791.

Kang, F., D.L. Purich, and F.S. Southwick. (1999). Profilin promotes barbed-end actin filament assembly without lowering the critical concentration. *J. Biol. Chem.* 274:36963–36972.

Katoh, K., M. Masuda, Y. Kano, K. Fujiwara, and Y. Jinguji. (1995). Focal adhesion proteins associated with apical stress fibers of human fibroblasts. *Cell Motil. Cytoskeleton*. 31:177–195.

Kiuchi, T., T. Nagai, K. Ohashi, N. Watanabe, and K. Mizuno. (2011). Live-cell imaging of G-actin dynamics using sequential FDAP. 1:240–244.

Kodera, N., D. Yamamoto, R. Ishikawa, and T. Ando. (2010). Video imaging of walking myosin V by high-speed atomic force microscopy. *Nature*. 468:72–6.

Krause, M., and A. Gautreau. (2014). Steering cell migration: Lamellipodium dynamics and the regulation of directional persistence. *Nat. Rev. Mol. Cell Biol.* 15:577–590.

Kuhn, J.R., and T.D. Pollard. (2005). Real-Time Measurements of Actin Filament Polymerization by Total Internal Reflection Fluorescence Microscopy. *Biophys. J.* 88:1387–1402.

Kühn, S., and M. Geyer. (2014). Formins as effector proteins of rho GTPases. *Small GTPases*. 5:1–16.

Kunda, P., A.E. Pelling, T. Liu, and B. Baum. (2008). Moesin Controls Cortical Rigidity, Cell Rounding, and Spindle Morphogenesis during Mitosis. *Curr. Biol.* 18:91–101.

Laevsky, G., and D.A. Knecht. (2003). Cross-linking of actin filaments by myosin II is a major contributor to cortical integrity and cell motility in restrictive environments. *J. Cell Sci.* 116:3761–3770.

Lai, F.P., M. Szczodrak, J. Block, J. Faix, D. Breitsprecher, H.G. Mannherz, T.E. Stradal, G.A. Dunn, J.V. Small, and K. Rottner. (2008). Arp2/3 complex interactions and actin network turnover in lamellipodia. *EMBO J.* 27:982–992.

Lebrand, C., E.W. Dent, G.A. Strasser, L.M. Lanier, M. Krause, T.M. Svitkina, G.G. Borisy, and F.B. Gertler. (2004). Critical role of Ena/VASP proteins for filopodia formation in neurons and in function downstream of netrin-1. *Neuron*. 42:37–49.

Li, K., Y. Zheng, and D.G. Drubin. (1995). Regulation of cortical actin cytoskeleton assembly during polarized cell growth in budding yeast. *J. Cell Biol.* 128:599–615.

Lin, T., L. Zeng, Y. Liu, K. DeFea, M.A. Schwartz, S. Chien, and J.Y.J. Shyy. (2003). Rho-ROCK-LIMK-cofilin pathway regulates shear stress activation of sterol regulatory element binding proteins. *Circ. Res.* 92:1296–1304.

Maddox, A.S., and K. Burridge. (2003). RhoA is required for cortical retraction and rigidity during mitotic cell rounding. *J. Cell Biol.* 160:255–265.

Maeda, M., H. Hasegawa, T. Hyodo, S. Ito, E. Asano, H. Yuang, K. Funasaka, K. Shimokata, Y. Hasegawa, M. Hamaguchi, and T. Senga. (2011). ARHGAP18, a GTPase-activating protein for RhoA, controls cell shape, spreading, and motility. *Mol. Biol. Cell*. 22:3840–3852.

Mallavarapu, A., and T. Mitchison. (1999). Regulated actin cytoskeleton assembly at filopodium tips controls their extension and retraction. *J. Cell Biol.* 146:1097–1106.

Mason, D.E., J.M. Collins, J.H. Dawahare, T.D. Nguyen, Y. Lin, S.L. Voytik-Harbin, P. Zorlutuna, M.C. Yoder, and J.D. Boerckel. (2019). YAP and TAZ limit cytoskeletal and focal adhesion maturation to enable persistent cell motility. *J. Cell Biol.* 218:1369–1389.

Matsui, T., S. Yonemura, S. Tsukita, and S. Tsukita. (1999). Activation of ERM proteins in vivo by Rho involves phosphatidylinositol 4-phosphate 5-kinase and not ROCK kinases. *Curr. Biol.* 9:1259–1262.

Michelot, A., E. Derivery, R. Paterski-Boujemaa, C. Guérin, S. Huang, F. Parcy, C.J. Staiger, and L. Blanchoin. (2006). A Novel Mechanism for the Formation of Actin-Filament Bundles by a Nonprocessive Formin. *Curr. Biol.* 16:1924–1930.

Morone, N., T. Fujiwara, K. Murase, R.S. Kasai, H. Ike, S. Yuasa, J. Usukura, and A. Kusumi. (2006). Three-dimensional reconstruction of the membrane skeleton at the plasma membrane interface by electron tomography. *J. Cell Biol.* 174:851–862.

Mullins, R.D., J.A. Heuser, and T.D. Pollard. (1998). The interaction of Arp2/3 complex with actin: Nucleation, high affinity pointed end capping, and formation of branching networks of filaments. *Proc. Natl. Acad. Sci. U. S. A.* 95:6181–6186.

Murthy, K., and P. Wadsworth. (2005). Myosin-II-dependent localization and dynamics of F-actin during cytokinesis. *Curr. Biol.* 15:724–731.

Nadkarni, A. V., and W.M. Brieher. (2014). Aip1 destabilizes cofilin-saturated actin filaments by severing and accelerating monomer dissociation from ends. *Curr. Biol.* 24:2749–2757.

Nagafuchi, A., and M. Takeichi. (1989). Transmembrane control of cadherin-mediated cell adhesion: a 94 kDa protein functionally associated with a specific region of the cytoplasmic domain of E-cadherin. *Cell Regul.* 1:37–44.

Nakamura, F., E. Osborn, P.A. Janmey, and T.P. Stossel. (2002). Comparison of filamin A-induced cross-linking and Arp2/3 complex-mediated branching on the mechanics of actin filaments. *J. Biol. Chem.* 277:9148–9154.

Panciera, T., L. Azzolin, M. Cordenonsi, and S. Piccolo. (2017). Mechanobiology of YAP and TAZ in physiology and disease V l. *Nat. Publ. Gr.* 18:758–770.

Pantaloni, D., and M.F. Carlier. (1993). How profilin promotes actin filament assembly in the presence of thymosin β4. *Cell.* 75:1007–1014.

Park, J.S., D.H. Kim, S.R. Shah, H.N. Kim, Kshitiz, P. Kim, A. Quiñones-Hinojosa, and A. Levchenko. (2019). Switch-like enhancement of epithelial-mesenchymal transition by YAP through feedback regulation of WT1 and Rho-family GTPases. *Nat. Commun.* 10:1–15.

Parsons, J.T., A.R. Horwitz, and M.A. Schwartz. (2010). Cell adhesion: Integrating cytoskeletal dynamics and cellular tension. *Nat. Rev. Mol. Cell Biol.* 11:633–643.

Pernier, J., S. Shekhar, A. Jegou, B. Guichard, and M.F. Carlier. (2016). Profilin Interaction with Actin Filament Barbed End Controls Dynamic Instability, Capping, Branching, and Motility. *Dev. Cell*. 36:201–214.

Pfisterer, K., J. Levitt, C.D. Lawson, R.J. Marsh, J.M. Heddleston, E. Wait, S.M. Ameer-Beg, S. Cox, and M. Parsons. (2020). FMNL2 regulates dynamics of fascin in filopodia. *J. Cell Biol.* 219.

Pollard, T.D. (1986). Rate constants for the reactions of ATP-and ADP-actin with the ends of actin filaments. *J. Cell Biol.* 103:2747.

Porazinski, S., H. Wang, Y. Asaoka, M. Behrndt, T. Miyamoto, H. Morita, S. Hata, T. Sasaki, S.F.G. Krens, Y. Osada, S. Asaka, A. Momoi, S. Linton, J.B. Miesfeld, B.A. Link, T. Senga, A. Castillo-Morales, A.O. Urrutia, N. Shimizu, H. Nagase, S. Matsuura, S. Bagby, H. Kondoh, H. Nishina, C.P. Heisenberg, and M. Furutani-Seiki. (2015a). YAP is essential for tissue tension to ensure vertebrate 3D body shape. *Nature*. 521:217–221.

Porazinski, S., H. Wang, Y. Asaoka, M. Behrndt, T. Miyamoto, H. Morita, S. Hata, T. Sasaki, S.F.G. Krens, Y. Osada, S. Asaka, A. Momoi, S. Linton, J.B. Miesfeld, B.A. Link, T. Senga, A. Castillo-Morales, A.O. Urrutia, N. Shimizu, H. Nagase, S. Matsuura, S. Bagby, H. Kondoh, H. Nishina, C.P. Heisenberg, and M. Furutani-Seiki. (2015b). YAP is essential for tissue tension to ensure vertebrate 3D body shape. *Nature*. 521:217–221.

Pruyne, D., M. Evangelista, C. Yang, E. Bi, S. Zigmond, A. Bretscher, and C. Boone. (2002). Role of formins in actin assembly: nucleation and barbed-end association. *Science*. 297:612–615.

Qiao, Y., J. Chen, Y.B. Lim, M.L. Finch-Edmondson, V.P. Seshachalam, L. Qin, T. Jiang, B.C. Low, H. Singh, C.T. Lim, and M. Sudol. (2017). YAP Regulates Actin Dynamics through ARHGAP29 and Promotes Metastasis. *Cell Rep.* 19:1495–1502.

Qualmann, B., M.M. Kessels, and R.B. Kelly. (2000). Molecular Links between Endocytosis and the Actin Cytoskeleton. *J. Cell Biol.* 150:111–116.

Quinlan, M.E., J.E. Heuser, E. Kerkhoff, and R.D. Mullins. (2005). Drosophila Spire is an actin nucleation factor. *Nature*. 433:382–388.

Rambhatla, L., C.P. Chiu, R.D. Glickman, and C. Rowe-Rendleman. (2002). In vitro differentiation capacity of telomerase immortalized human RPE cells. *Investig. Ophthalmol. Vis. Sci.* 43:1622–1630.

Ridley, A.J. (2006). Rho GTPases and actin dynamics in membrane protrusions and vesicle trafficking. *Trends Cell Biol.* 16:522–529.

Riedl, J., A.H. Crevenna, K. Kessenbrock, J.H. Yu, D. Neukirchen, M. Bista, F. Bradke, D. Jenne, T.A. Holak, Z. Werb, M. Sixt, and R. Wedlich-Soldner. (2008). Lifeact: A versatile marker to visualize F-actin. *Nat. Methods*. 5:605–607.

Ryan, G.L., H.M. Petroccia, N. Watanabe, and D. Vavylonis. (2012). Excitable actin dynamics in lamellipodial protrusion and retraction. *Biophys. J.* 102:1493–1502.

Sakamoto, S., D. Thumkeo, H. Ohta, Z. Zhang, S. Huang, P. Kanchanawong, T. Fuu, S. Watanabe, K. Shimada, Y. Fujihara, S. Yoshida, M. Ikawa, N. Watanabe, M. Saitou, and S. Narumiya. (2018). mDia1/3 generate cortical F-actin meshwork in Sertoli cells that is continuous with contractile F-actin bundles and indispensable for spermatogenesis and male fertility. *PLoS Biol.* 16:1–30.

Schirenbeck, A., R. Arasada, T. Bretschneider, T.E.B. Stradal, M. Schleicher, and J. Faix. (2006). The bundling activity of vasodilator-stimulated phosphoprotein is required for filopodium formation. *Proc. Natl. Acad. Sci. U. S. A.* 103:7694–7699.

Shah, S.R., N.D. Tippens, J. Park, A. Mohyeldin, S. Wang, G. Vela, J.C. Martinez-Gutierrez, S.S. Margolis, S. Schmidt, S. Xia, A. Levchenko, and A. Quiñones-Hinojosa. (2019). YAP controls cell migration and invasion through a Rho-GTPase switch. *bioRxiv*.

Smythe, E., and K.R. Ayscough. (2006). Actin regulation in endocytosis. *J. Cell Sci.* 119:4589–4598.

Stewart, M.P., J. Helenius, Y. Toyoda, S.P. Ramanathan, D.J. Muller, and A.A. Hyman. (2011). Hydrostatic pressure and the actomyosin cortex drive mitotic cell rounding. *Nature*. 469:226–231.

Stroetz, R.W., N.E. Vlahakis, B.J. Walters, M.A. Schroeder, and R.D. Hubmayr. (2001). Validation of a new live cell strain system: Characterization of plasma membrane stress failure. *J. Appl. Physiol.* 90:2361–2370.

Suraneni, P., B. Rubinstein, J.R. Unruh, M. Durnin, D. Hanein, and R. Li. (2012). The Arp2/3 complex is required for lamellipodia extension and directional fibroblast cell migration. *J. Cell Biol.* 197:239–251.

Suzuki, Y., N. Sakai, A. Yoshida, Y. Uekusa, A. Yagi, Y. Imaoka, S. Ito, K. Karaki, and K. Takeyasu. (2013). High-speed atomic force microscopy combined with inverted optical microscopy for studying cellular events. *Sci. Rep.* 3:2131.

Svitkina, T. (2018). The actin cytoskeleton and actin-based motility. *Cold Spring Harb. Perspect. Biol.* 10:1–21.

Svitkina, T.M., E.A. Bulanova, O.Y. Chaga, D.M. Vignjevic, S. ichiro Kojima, J.M. Vasiliev, and G.G. Borisy. (2003). Mechanism of filopodia initiation by reorganization of a dendritic network. *J. Cell Biol.* 160:409–421.

Takayuki, U., I. Ryota, A. Toshio, and N. Hiroyuki. (2011). High-Speed Atomic Force Microscopy Reveals Rotary Catalysis of Rotorless F1-ATPase. 755–758.

Thoumine, O., O. Cardoso, and J.J. Meister. (1999). Changes in the mechanical properties of fibroblasts during spreading: A micromanipulation study. *Eur. Biophys. J.* 28:222–234.

Tinevez, J.Y., N. Perry, J. Schindelin, G.M. Hoopes, G.D. Reynolds, E. Laplantine, S.Y. Bednarek, S.L. Shorte, and K.W. Eliceiri. (2016). TrackMate: An open and extensible platform for single-particle tracking. *Methods*. 115:80–90.

Tojkander, S., G. Gateva, and P. Lappalainen. (2012). Actin stress fibers - assembly, dynamics and biological roles. *J. Cell Sci.* 125:1855–1864.

Vavylonis, D., D.R. Kovar, B. O'Shaughnessy, and T.D. Pollard. (2006). Model of Formin-Associated Actin Filament Elongation. *Mol Cell.* 21:455–466.

Wada, K.-I., K. Itoga, T. Okano, S. Yonemura, and H. Sasaki. (2011). Hippo pathway regulation by cell morphology and stress fibers. *Development*. 138:3907–3914.

Watanabe, N., and T.J. Mitchison. (2002). Single-molecule speckle analysis of actin filament turnover in lamellipodia. *Science (80-.).* 295:1083–6.

Wear, M.A., A. Yamashita, K. Kim, Y. Mae´da, and J.A. Cooper. (2003). How Capping Protein Binds the Barbed End of the Actin Filament. *Curr. Biol.* 13:1531–1537.

Wulf, E., A. Deboben, F.A. Bautz, H. Faulstich, and T. Wieland. (1979). Fluorescent phallotoxin, a tool for the visualization of cellular actin. *Proc. Natl. Acad. Sci. U. S. A.* 76:4498–4502.

Xu, Y., J.B. Moseley, I. Sagot, F. Poy, D. Pellman, B.L. Goode, and M.J. Eck. (2004). Crystal structures of a formin homology-2 domain reveal a tethered dimer architecture. *Cell*. 116:711–723.

Yagi, R., L.F. Chen, K. Shigesada, Y. Murakami, and Y. Ito. (1999). A WW domain-containing Yes-associated protein (YAP) is a novel transcriptional co-activator. *EMBO J.* 18:2551–2562.

Yamashiro, S., H. Mizuno, M.B. Smith, G.L. Ryan, T. Kiuchi, D. Vavylonis, and N. Watanabe. (2014). New single-molecule speckle microscopy reveals modification of the retrograde actin flow by focal adhesions at nanometer scales. *Mol. Biol. Cell*. 25:1010–1024.

Yang, C., L. Czech, S. Gerboth, S.I. Kojima, G. Scita, and T. Svitkina. (2007). Novel roles of formin mDia2 in lamellipodia and filopodia formation in motile cells. *PLoS Biol.* 5:2624–2645.

Yoshida, A., N. Sakai, Y. Uekusa, K. Deguchi, J.L. Gilmore, M. Kumeta, S. Ito, and K. Takeyasu. (2015). Probing in vivo dynamics of mitochondria and cortical actin

networks using high-speed atomic force/fluorescence microscopy. *Genes to Cells*. 20:85–94.

Yu, F.X., S.C. Lin, M. Morrison-Bogorad, M.A.L. Atkinson, and H.L. Yin. (1993). Thymosin β10 and thymosin β4 are both actin monomer sequestering proteins. *J. Biol. Chem.* 268:502–509.

Zhao, B., B. Zhao, X. Wei, X. Wei, W. Li, W. Li, R.S. Udan, R.S. Udan, Q. Yang, Q. Yang, J. Kim, J. Kim, J. Xie, J. Xie, T. Ikenoue, T. Ikenoue, J. Yu, J. Yu, L. Li, L. Li, P. Zheng, P. Zheng, K. Ye, K. Ye, A. Chinnaiyan, A. Chinnaiyan, G. Halder, G. Halder, Z. Lai, Z. Lai, K.-L. Guan, and K.-L. Guan. (2007). Inactivation of YAP oncoprotein by the Hippo pathway is involved in cell contact inhibition and tissue growth control. *Genes Dev.* 21:2747–2761.

Acknowledgments

First, I would like to express my sincere gratitude to my supervisor Prof. Yoshimura Shigehiro for providing me the opportunity for Ph. D. study in his lab. His continuous support, valuable discussions, and humorous personality broadened my mind, helped me grow during the entire doctoral course. The thinking about research learned from him will be with me even after I leave this lab. I also want to thank Prof. Kumeta Masahiro. His helpful advices, optimistic personality helped and encouraged me to solve many problems. My sincere thank also goes to Prof. Seiki in Yamaguchi University, Nobuaki Sakai, Yoshitsugu Uekusa in Olympus for launching the project and providing excellent equipment. I'm also grateful to Dr. Yoshida Aiko, Yoshitsuna Itagaki for the technical training and support in HS-AFM, Wanzhen Zhang, for the experimental support. I want to thank all the members in Yoshimura lab. I thank Takako Fukuda, Satsuki Dodo, Nur Diyana Binti Maarof for their kindness and encouragement. Last but not the least, I would like to thank my parents, my family for their support during my doctoral course and my life.

This thesis is based on material contained in the following scholarly paper:

Yanshu Zhang, Aiko Yoshida, Nobuaki Sakai, Yoshitsugu Uekusa, Masahiro Kumeta, Shige H. Yoshimura

In vivo dynamics of the cortical actin network revealed by fast-scanning atomic force microscopy

Microscopy, Vol. 66, No.4, 272-282, 2017